Title

Structure of LRRK2 in Parkinson’s disease and model for microtubule interaction

Journal

Nature, 588(7837)

ISSN

0028-0836

Authors

Deniston, CK
Salogiannis, J
Mathea, S
et al.

Publication Date

2020-12-10

DOI

10.1038/s41586-020-2673-2

Peer reviewed

HHS Public Access

Author manuscript

Nature. Author manuscript; available in PMC 2021 February 19.

Published in final edited form as:

Nature. 2020 December ; 588(7837): 344–349. doi:10.1038/s41586-020-2673-2.

Structure of LRRK2 in Parkinson's disease and model for microtubule interaction

CK Deniston[1,*], **J Salogiannis**[1,2,*], **S Mathea**[3,*], **DM Snead**[1], **I Lahiri**[1,4], **M Matyszewski**[1], **O Donosa**[2], **R Watanabe**[5,6], **J Böhning**[5,7], **AK Shiau**[8,9], **S Knapp**[3], **E Villa**[5], **SL Reck-Peterson**[1,2,9,#], **AE Leschziner**[1,5,#]

[1]Department of Cellular and Molecular Medicine, University of California San Diego, La Jolla CA, USA

[2]Howard Hughes Medical Institute, Chevy Chase MD, USA

[3]Institute of Pharmaceutical Chemistry, Goethe-Universität, Frankfurt, Germany

[4]Present address: Department of Biological Sciences, Indian Institute of Science Education and Research Mohali, Mohali, Punjab, India

[5]Division of Biological Sciences, Molecular Biology Section, University of California San Diego, La Jolla CA, USA

[6]Present address: La Jolla Institute for Immunology, La Jolla CA, USA

[7]Present address: Sir William Dunn School of Pathology, Oxford University, Oxford, UK

[8]Small Molecule Discovery Program, Ludwig Institute for Cancer Research, La Jolla CA, USA

[9]Division of Biological Sciences, Cell and Developmental Biology Section, University of California San Diego, La Jolla CA, USA

Summary

Leucine **R**ich **R**epeat **K**inase **2** (*LRRK2*) is the most commonly mutated gene in familial Parkinson's disease (PD)[1] and is also linked to its idiopathic form[2]. LRRK2 is proposed to function in membrane trafficking[3] and co-localizes with microtubules[4]. Despite LRRK2's fundamental importance for understanding and treating PD, there is limited structural information on it. Here we report the 3.5Å structure of the catalytic half of LRRK2, and an atomic model of

[#]Co-corresponding authors Correspondence and material requests can be made to either AEL (aleschziner@ucsd.edu) or SLR-P (sreckpeterson@ucsd.edu).

[*]Equal contribution

AUTHOR CONTRIBUTIONS

CKD collected and processed the cryo-EM data. JS performed the single-molecule and cellular assays with the help of OD. SM designed the LRRK2^{RCKW} construct and purified the protein. CKD and IL built the molecular model of LRRK2^{RCKW}. DS performed the SEC-MALS and phosphorylation assays. MM collected and analyzed the LRRK2^{RCKW} and microtubule cryo-EM data. RW and JB performed the cellular cryo-ET. AKS contributed to the structural analysis and provided advice on the selection of kinase inhibitors. SK, EV, SLR-P and AEL directed and supervised the research. CKD, JS, SLR-P and AEL wrote the manuscript and SM, DS, MM, OD, AKS, SK and EV edited it.

COMPETING INTERESTS

The authors have no competing interests to declare.

microtubule-associated LRRK2 built using a reported 14Å cryo-electron tomography *in situ* structure[5]. We propose that the conformation of LRRK2's kinase domain regulates its microtubule interaction, with a closed conformation favoring oligomerization on microtubules. We show that the catalytic half of LRRK2 is sufficient for filament formation and blocks the motility of the microtubule-based motors kinesin-1 and cytoplasmic dynein-1 *in vitro*. Kinase inhibitors that stabilize an open conformation relieve this interference and reduce LRRK2 filament formation in cells, while those that stabilize a closed conformation do not. Our findings suggest that LRRK2 can act as a roadblock for microtubule-based motors and have implications for the design of therapeutic LRRK2 kinase inhibitors.

LRRK2 is a large (288 kDa) multi-domain protein. Its amino-terminal half is comprised of repetitive protein interaction motifs (Armadillo, Ankyrin, and Leucine-Rich Repeats) and its carboxy-terminal catalytic half contains a Ras-like GTPase (Ras-of-Complex, or RoC domain), a kinase domain, and two other domains (C-terminal Of Roc, or COR, and WD40) (Fig. 1a). High-resolution structural data on LRRK2 is limited to bacterial homologs[6,7] or isolated domains[8,9], whereas low resolution full-length protein structures have been obtained using negative stain[10] and cryo-electron microscopy (Cryo-EM)[11]. A recent study of LRRK2 bound to microtubules in cells using cryo-electron tomography (Cryo-ET) and subtomogram analysis led to a 14Å structure and proposed model of the catalytic half of LRRK2[5].

LRRK2's interaction with microtubules is linked to disease as four of the five major PD-causing mutations (Fig. 1a)[1] enhance microtubule association of LRRK2[12]. Further, Rab GTPases, which mark membranous cargos that move along microtubules, are physiological LRRK2 kinase substrates[13,14]. These cargos, and others implicated in PD pathology[3], are transported by the microtubule-based motors dynein and kinesin. Here, we set out to determine a high-resolution structure of LRRK2's catalytic half using cryo-EM, and to understand how it interacts with microtubules and how this impacts microtubule-based motor movement.

Structure of the catalytic half of LRRK2

High-resolution studies on human LRRK2 have been limited by the lack of efficient expression systems that yield stable protein. We tested many constructs (Extended Data Fig. 1a), leading to the identification of one consisting of the carboxy-terminal half of wild-type (WT) LRRK2 (amino acids 1,327 to 2,527), which resulted in robust insect cell expression and well-behaved protein (Extended Data Fig. 1b, c). This construct comprises the **R**oC, **C**OR, **k**inase and **W**D40 domains of LRRK2 (Fig. 1a), which we refer to as LRRK2^{RCKW}. The COR domain was previously defined as consisting of two subdomains, COR-A and COR-B[6].

We determined a 3.5Å structure of LRRK2^{RCKW} in the presence of GDP using cryo-EM (Fig. 1b, c and Extended Data Figs. 1 and 2). On our grids, we observed a mixture of monomers, dimers and head-to-tail trimers; we used the trimer to solve the structure (Fig. 1b and Extended Data Figs. 1 and 2). Although critical for reaching high resolution, the trimer is likely specific to the cryo-EM grid preparation as LRRK2^{RCKW} is predominantly

monomeric, with a smaller percentage of dimers, in solution (Extended Data Fig. 2n) and we only observed the trimer when preparing grids with high concentrations of LRRK2^{RCKW} (see Methods). Due to flexibility, the RoC and COR-A domains were lower resolution in our structure (Fig. 1b, c). We improved this part of the map using signal subtraction and focused 3D classification and refinement (Fig. 1d, e, Extended Data Figs. 2a-d). The final model was generated using the signal subtracted maps of the RoC and COR-A domains, and then combined with the COR-B, kinase and WD40 domains from the trimer map (Fig. 1f, Extended Data Fig. 2e-m and Supplementary Video 1). Our model fits well into an 8.1Å reconstruction we obtained of a LRRK2^{RCKW} monomer (Fig. 1g, and see Extended Data Fig. 6), indicating that trimer formation does not cause major structural changes in the protein.

LRRK2^{RCKW} adopts an overall J-shape, with the WD40, kinase and COR-B domains arranged along one axis, and COR-A and RoC turning around back towards the kinase. This brings the COR-A and tightly associated RoC domain into close proximity to the kinase's C-lobe (Fig. 1f, and Supplementary Video 1). This arrangement likely underpins the crosstalk between LRRK2's kinase and GTPase[15,16]. Part of the FERM domain in the FAK-FERM complex approaches the FAK C-lobe in a similar way[17] (Extended Data Fig. 3a, b). The RoC, COR-A and COR-B domains are arranged as seen in crystal structures of LRRK2 bacterial homologs[6,7,18]. The N-lobe of the kinase domain, in particular its αC helix, forms an extensive interaction with the COR-B domain, with COR-B occupying a location similar to Cyclin A in CDK2-Cyclin A[19] (Extended Data Fig. 3a, c).

The kinase in our LRRK2^{RCKW} structure is in an open, inactive conformation. Its activation loop contains the site of two familial PD mutations (G2019S and I2020T) and is disordered beyond G2019 (Fig. 1h, Extended Data Fig. 2h, and Supplementary Video 2). R1441 and Y1699 are the sites of three other familial PD mutations and are located at the RoC-COR-B interface (Fig. 1h, Extended Data Fig. 2j, and Supplementary Video 2). Given that the kinase and GTPase interact with each other via the COR-A domain, it is possible that these mutations, located at the interface between the GTPase and COR-B, alter the conformational landscape of LRRK2 in response to ligands and/or regulatory signals and thus affect the cross-talk between LRRK2's catalytic domains.

A unique feature of LRRK2 is a 28-amino acid α-helix located at its extreme C-terminus, following the WD40 domain (Fig. 1i, j, and Supplementary Video 3). While a number of other kinases have α-helices in the same general location, none form interactions as extensive as those observed in LRRK2 (Fig. 1i, j, Extended Data Fig. 3d-i). Deletion of this helix resulted in an insoluble protein (Extended Data Fig. 1a, b). A residue near its end (T2524) is a known phosphorylation site for LRRK2[20]. Given the close proximity between T2524 and the N-lobe of the kinase domain, as well as the adjacent COR-B domain, we hypothesize that phosphorylation of this residue may play a role in regulating the kinase. Since the last two residues of the C-terminal helix are disordered in our structure, as is a neighboring loop in COR-B, it is possible that conditions exist where these regions become ordered and turn the C-terminal helix into a scaffolding element that connects COR-B, the kinase and the WD40 domains.

We modeled the Leucine-Rich Repeats (LRR) into LRRK2^{RCKW} by using a crystal structure of the LRR, RoC, and COR domains of *C. tepidum*'s Roco protein[7] (Extended Data Fig. 3l-p). In our model, the LRR wraps around the N-lobe of the kinase and approaches the C-lobe, placing the known S1292 autophosphorylation site in the LRR close to the kinase's active site, and the Crohn's disease-associated residue N2081[21], located in the kinase's C-lobe, next to the LRR (Extended Data Fig. 3q), suggesting the functional relevance of this predicted interface.

Model of microtubule-bound filaments

Recently, a 14Å structure of microtubule-associated filaments of full-length LRRK2 (carrying the filament-promoting I2020T mutation[12]) was determined using *in situ* cryo-ET and subtomogram analysis[5] (Fig. 2a). The LRRK2 filaments formed on microtubules are right-handed[5]. Because microtubules are left-handed and no strong density connected the LRRK2 filament to the microtubule surface[5], it is unknown if LRRK2's microtubule interaction is direct. To address this, we combined purified microtubules and LRRK2^{RCKW}, either WT or I2020T, and imaged them by cryo-EM. Both WT and I2020T LRRK2^{RCKW} bound to microtubules, and diffraction patterns calculated from the images revealed layer lines consistent with the formation of ordered filaments (Fig. 2b). Thus, the interaction between LRRK2 and microtubules is direct and the catalytic C-terminal half of LRRK2 is sufficient for the formation of microtubule-associated filaments. The layer line patterns of WT and I2020T LRRK2^{RCKW} are different, with the I2020T diffraction pattern having an additional layer line of lower frequency, indicating longer-range order in the filaments (Fig. 2b). This is consistent with the observation that the I2020T mutation promotes microtubule association by LRRK2 in cells[12]. Understanding the structural basis for this effect will require high-resolution structures of the filaments formed by WT and I2020T LRRK2.

Previously, integrative modeling was used to build a model into the *in situ* structure of microtubule-associated LRRK2[5]. This modeling indicated that the well-resolved Cryo-ET density closest to the microtubule was comprised of the RoC, COR, Kinase and WD40 domains and gave orientation ensembles for each domain[5] that are in good agreement with our high-resolution structure of LRRK2^{RCKW} (Extended Data Fig. 4a). Here, we built an atomic model of the microtubule-bound LRRK2 filaments by combining our 3.5Å structure of LRRK2^{RCKW} with the 14Å *in situ* structure of microtubule-associated LRRK2 (Extended Data Fig. 4b-f). This revealed that the LRRK2^{RCKW} structure is sufficient to account for the density seen in the *in situ* structure (Fig. 2c), in agreement with our ability to reconstitute microtubule-associated LRRK2^{RCKW} filaments *in vitro* (Fig. 2b), and with the earlier modeling[5].

Although our LRRK2^{RCKW} structure fits the overall shape of the cryo-ET map, there were significant clashes at the COR domain interfaces (Fig. 2d). Since the kinase in our LRRK2^{RCKW} structure is in an open conformation, we hypothesized that filament formation might require LRRK2's kinase to be in a closed conformation. To test this, we modeled a kinase-closed LRRK2^{RCKW} (Fig. 2e and Extended Data Fig. 4g-j) and used it to rebuild the LRRK2 filament. The kinase-closed LRRK2^{RCKW} model resolved more than 80% of the backbone clashes we had observed with our kinase-open LRRK2^{RCKW} structure (Fig. 2c, d,

f, g). A closed conformation for the kinase was also proposed by the integrative modeling[5]. Given this data, we hypothesize that the conformation of LRRK2 controls its ability to oligomerize on microtubules, with a closed kinase promoting oligomerization and an open (inactive) one disfavoring it (Fig. 2h, i).

The LRRK2 filaments in our kinase-closed model are formed by two homotypic interactions: one is mediated by the WD40 domain, and the other by the COR-A and COR-B domains (Fig. 3a-d). Similar interfaces were reported based on the cryo-ET structure[5]. We also solved structures of LRRK2^{RCKW} dimers, using the same grids that yielded the 3.5Å structure of LRRK2^{RCKW}. We obtained structures of both the WD40/WD40- and COR/COR-mediated dimers, indicating that both interfaces mediate dimerization in the absence of microtubules (Fig. 3e, f and Extended Data Figs. 5 and 6). The interface in the COR-mediated dimer of LRRK2^{RCKW} differs from that reported for the *C. tepidum* Roco protein[6,7]; while the GTPase domains interact directly in the dimer of the bacterial protein[7], they are not involved in the dimerization interface we observed for LRRK2 (Extended Data Fig. 6c).

We built an independent model of a closed-kinase LRRK2^{RCKW} by splitting our 3.5Å structure in half at the junction between the N- and C-lobes of the kinase, and fitting the fragments into our cryo-EM map of a WD40/WD40 dimer obtained in the presence of a LRRK2-specific Type I kinase inhibitor, MLi-2[22,23], which is predicted to stabilize the kinase closed conformation (Extended Data Fig. 7a-c). We then docked this closed-kinase model (Extended Data Fig. 7c) into the cryo-EM maps of WD40- and COR-mediated dimers obtained in the presence of MLi-2 to generate molecular models of both dimers (Extended Data Fig. 7d, e). We aligned these models to build a polymer *in silico*. This resulted in a right-handed helix with the same general geometric properties seen in the cellular LRRK2 filaments, indicating that those properties are largely encoded in the structure of LRRK2^{RCKW} itself (Fig. 3g, h, and Extended Data Fig. 7f). Docking the same two halves of LRRK2^{RCKW} into the cryo-EM map of a monomer we obtained in the absence of inhibitors or ATP led to a structure similar to our 3.5Å structure obtained from trimers, further confirming that trimer formation does not alter the conformation of LRRK2^{RCKW} (Extended Data Fig. 7g, h).

These data, along with the apparent lack of any residue-specific interactions between LRRK2 and the microtubule lattice, suggest that the microtubule may provide a surface for LRRK2 to oligomerize on using interfaces that exist in solution, thus explaining the symmetry mismatch between the microtubule and the LRRK2 filament. Consistent with this, the surface charge of the microtubule facing the LRRK2^{RCKW} filament is acidic, while there are basic patches on the LRRK2^{RCKW} filament facing the microtubule (Extended Data Fig. 7i-l). The unstructured C-terminal tails of α- and β-tubulin, which were not included in the surface charge calculations, are also acidic.

LRRK2^{RCKW} inhibits kinesin and dynein

To test our hypothesis that the conformation of LRRK2's kinase domain regulates its interaction with microtubules, we needed a sensitive assay to measure the association of

LRRK2^{RCKW} with microtubules and a means to control the conformation of its kinase. We monitored microtubule association by measuring the effect of LRRK2^{RCKW} on microtubule-based motor motility. We used a truncated human kinesin-1, Kif5B ("kinesin")[24], which moves towards the microtubule plus end, and the activated human cytoplasmic dynein-1/ dynactin/ ninein-like complex ("dynein")[25], which moves in the opposite direction. Using single-molecule *in vitro* motility assays (Fig. 4a), we found that low nanomolar concentrations of LRRK2^{RCKW} inhibited both kinesin and dynein movement, with near complete inhibition at 25 nM LRRK2^{RCKW} (Fig. 4b, c and Extended Data Fig. 8a, b). We hypothesized that LRRK2^{RCKW} was acting as a roadblock for the motors. In agreement with this, the distance that single kinesins moved (run length) was reduced (Fig. 4d), while their velocity remained relatively constant (Fig. 4e). We obtained similar results with dynein (Fig. 4f). Other microtubule-associated proteins, such as MAP2 and Tau, also inhibit kinesin, but not dynein[26,27], likely due to dynein's ability to sidestep on the microtubule[28-30]. LRRK2's unusual ability to inhibit dynein may be a consequence of it forming oligomers that cannot be overcome by sidestepping.

We also tested the inhibition of kinesin by I2020T LRRK2^{RCKW}, which promotes filament formation when overexpressed in cells[12]. I2020T LRRK2^{RCKW} inhibited kinesin to a similar extent as WT LRRK2^{RCKW} (Extended Data Fig. 8c, d). Given that *in vitro* reconstituted filaments of I2020T LRRK2^{RCKW} show longer range order compared with WT LRRK2^{RCKW} (Fig. 2b), it is possible that the high sensitivity of the single-molecule motility assays does not allow us to distinguish differences in oligomer length and/or stability between WT and I2020T LRRK2^{RCKW}.

Type II inhibitors rescue the motors

Our hypothesis predicts that the closed conformation of LRRK2's kinase domain will favor LRRK2's oligomerization on microtubules. Conversely, it predicts that conditions that stabilize the kinase in an open conformation will prevent oligomerization and thus decrease microtubule binding by LRRK2^{RCKW}, resulting in relief of LRRK2^{RCKW}-dependent inhibition of kinesin and dynein motility. To test these predictions, we searched for a Type II kinase inhibitor that binds tightly to LRRK2 with structural evidence that it stabilizes an open kinase conformation. We selected Ponatinib, which has a K_i for LRRK2 of 31 nM[31], and crystal structures show it bound to RIPK2[32] and IRAK4 (PDB: 6EG9) in open conformations (Extended Data Fig. 9a). Ponatinib inhibited LRRK2^{RCKW}'s ability to phosphorylate Rab8a[13] (Extended Data Fig. 9f).

As our hypothesis predicted, Ponatinib rescued kinesin motility in a dose-dependent manner at concentrations of LRRK2^{RCKW} (25 nM) that had resulted in almost complete inhibition of kinesin (Fig. 5a, Extended Data Fig. 9g-j). We observed similar effects with GZD-824, a chemically-related Type II kinase inhibitor[33] (Fig. 5a and Extended Data Fig. 9i, j). Our hypothesis also predicted that kinase inhibitors that stabilize the closed form of the kinase would not rescue the motors and might enhance the inhibitory effect of LRRK2^{RCKW} by increasing its ability to form filaments on microtubules. Indeed, MLi-2[22,23] and another LRRK2-specific Type I inhibitor, LRRK2-IN-1[34], which are expected[22,35] to stabilize a closed conformation of the kinase (Extended Data Fig. 9b-e), further enhanced the inhibitory

activity of LRRK2^{RCKW} on kinesin (Fig. 5a). Dynein motility was also rescued by Ponatinib and GZD-824, but not by MLi-2 or LRRK2-IN-1 (Fig. 5b, Extended Data Fig. 9i, k). Like Ponatinib, GZD-824, MLi-2 and LRRK2-IN-1 inhibited phosphorylation of Rab8a by LRRK2^{RCKW} (Extended Data Fig. 9f).

GZD-824 reduces filaments in cells

In cells, LRRK2 forms filaments that colocalize with a subset of microtubules and are sensitive to the microtubule depolymerizing drug nocodazole[12]. This association is enhanced by the PD-linked mutations R1441C, R1441G, Y1699C and I2020T[12,36] and by Type I kinase inhibitors[34,37]. We tested our kinase conformation hypothesis in human 293T cells by determining if Type I and Type II kinase inhibitors had opposite effects on the formation of microtubule-associated LRRK2 filaments in cells. Consistent with previous findings[37,38], the Type I inhibitor MLi-2 enhanced LRRK2's microtubule association (Fig. 5c), suggesting that the closed conformation of the kinase favors binding to microtubules in cells. In contrast, we found that the Type II inhibitor GZD-824 reduced the filament-forming ability of overexpressed LRRK2 (I2020T) (Fig. 5d). This reduction in LRRK2 filament formation was not due to changes in LRRK2 protein expression levels or the overall architecture of the microtubule cytoskeleton (Extended Data Fig. 9l-n).

Conclusions

Here we reported the 3.5Å structure of the catalytic half of LRRK2 and used it, in combination with a 14Å cryo-ET structure of microtubule-associated LRRK2 filaments[5], to build an atomic model of these filaments. This modeling led us to hypothesize that the conformation of LRRK2's kinase controls its association with microtubules (Fig. 5e). Cryo-EM structures of LRRK2^{RCKW} dimers we obtained in the absence of microtubules showed that the same interfaces are involved in both dimerization and filament formation, and aligning them *in silico* resulted in a right-handed filament with similar properties to LRRK2 filaments observed in cells, suggesting that the ability of LRRK2 to form filaments is a property inherent to LRRK2, and specifically the RCKW domains. We propose that both the surface charge and geometric complementarity between the microtubule and LRRK2 promote the formation of LRRK2 filaments. It remains to be determined whether LRRK2^{RCKW} monomers or dimers are the minimal filament forming unit.

We tested our model that the conformation of LRRK2's kinase regulates microtubule association using kinase inhibitors expected to stabilize either the open (Type II) or closed (Type I) conformations of the kinase. In support of our model, Type II inhibitors relieved the LRRK2^{RCKW}-dependent inhibition of kinesin and dynein and reduced LRRK2 filament formation in cells, while Type I inhibitors failed to rescue motor motility and enhanced filament formation in cells. Importantly, our single-molecule motility assays showed that low nanomolar concentrations of LRRK2^{RCKW} negatively impact both kinesin and dynein. At these low concentrations it is likely that LRRK2 would not form the long, highly ordered filaments and microtubule bundles observed in cells overexpressing the protein; instead, we hypothesize that at endogenous expression levels in cells LRRK2 forms short oligomers on microtubules.

What is the physiological role of non-pathogenic microtubule-associated LRRK2? Our data show that LRRK2 acts as a roadblock for microtubule-based motors *in vitro*. In cells, dynein and kinesin bind directly or indirectly to many Rab-marked cargos[39-43]. Our data also show that the microtubule-associated form of LRRK2 has its kinase in a closed (and potentially active) conformation. Given this, microtubule-associated LRRK2 stalling of kinesin or dynein could increase the likelihood that LRRK2 phosphorylates cargo-associated Rabs[13], modulating effector binding[13] and resulting in changes in cargo dynamics. In support of this, the four PD mutations that enhance LRRK2 microtubule binding[12] also show higher levels of Rab phosphorylation in cells than the G2019S mutant[13,14], whose microtubule binding is not enhanced over wild-type LRRK2[12].

Our data have important implications for the design of LRRK2 kinase inhibitors for therapeutic purposes. They predict that inhibitors that favor the closed conformation of the kinase will promote LRRK2 filament formation, thus blocking microtubule-based trafficking, while inhibitors that favor an open conformation of the kinase will not. These results should be taken into account to enhance therapeutically beneficial effects of LRRK2 kinase inhibition and to avoid potential unintended side effects.

Extended Data

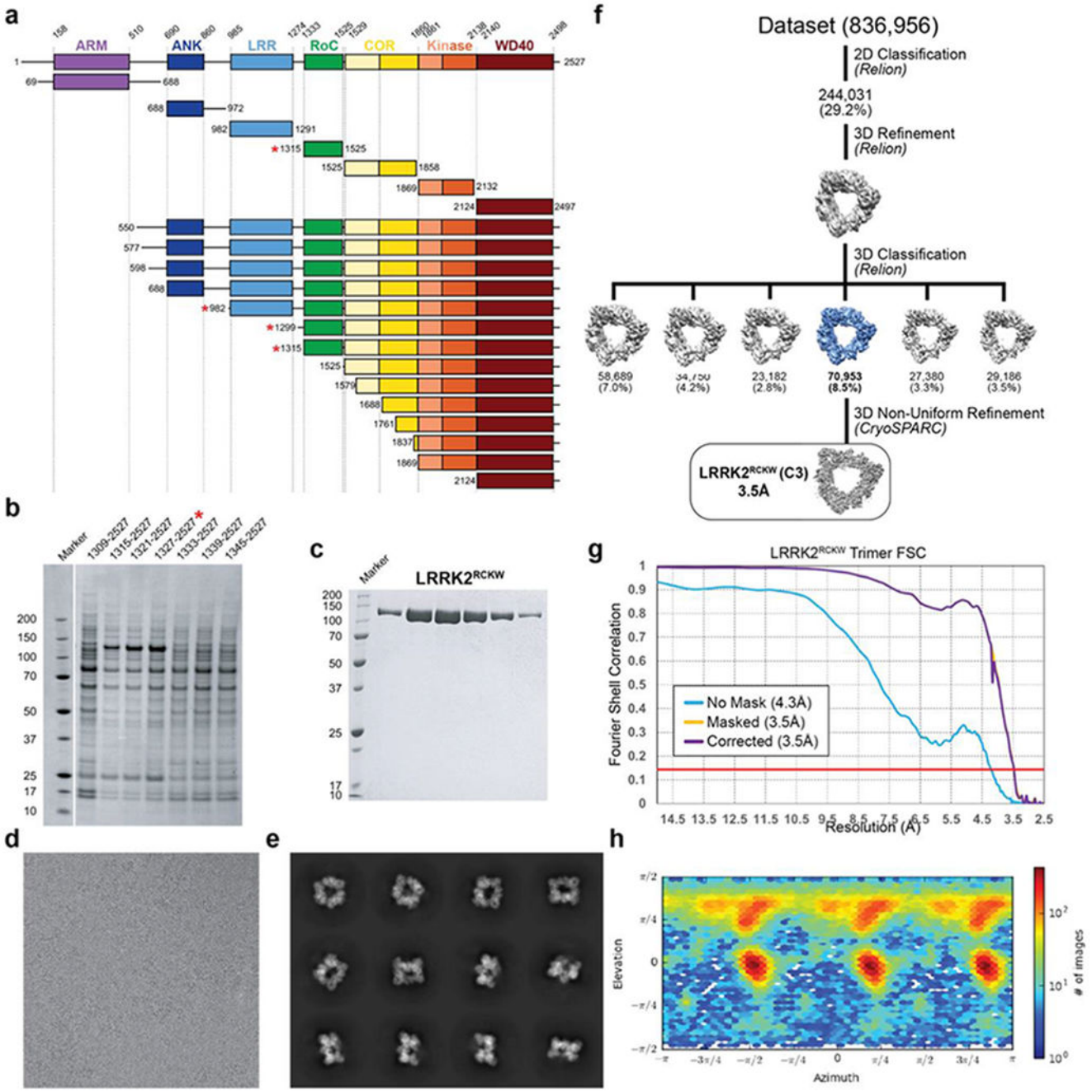

Extended Data Figure 1 |. Optimization of LRRK2 constructs and cryo-EM analysis of a LRRK2^{RCKW} trimer.

a, We systematically scanned domain boundaries (amino acid numbers of boundaries noted above domain names) to generate LRRK2 constructs that expressed well in baculovirus-infected insect cells and yielded stable and soluble protein. These attempts included full-length LRRK2, the kinase domain alone or with the WD40 domain, and other isolated domains. In this approach, only the GTPase domain on its own expressed well. Next, we

gradually shortened LRRK2 from its amino-terminus. Red asterisks indicate constructs that were soluble. **b,** After identifying domain boundaries yielding constructs that expressed soluble protein, additional fine tuning of boundaries was performed. A Coomassie stained SDS-PAGE gel shows systematic N-terminal truncations at the RoC domain resulting in the identification of a construct with the highest expression levels: amino acids 1327 to 2527 (red asterisk, "LRRK2^{RCKW}" here). **c,** A Coomassie stained SDS-PAGE gel of purified LRRK2^{RCKW} after elution from an S200 gel filtration column. As predicted by its primary structure, LRRK2^{RCKW} runs at ~140 kDa. **d**, Electron micrograph of LRRK2^{RCKW}. **e**, 2D class averages of the LRRK2^{RCKW} trimer. **f**, 2D/3D classification scheme used to obtain the 3.5Å structure of the LRRK2^{RCKW} trimer. **g, h,** Fourier Shell Correlations (from Cryosparc) (d) and Euler angle distribution (e) for the LRRK2^{RCKW} trimer.

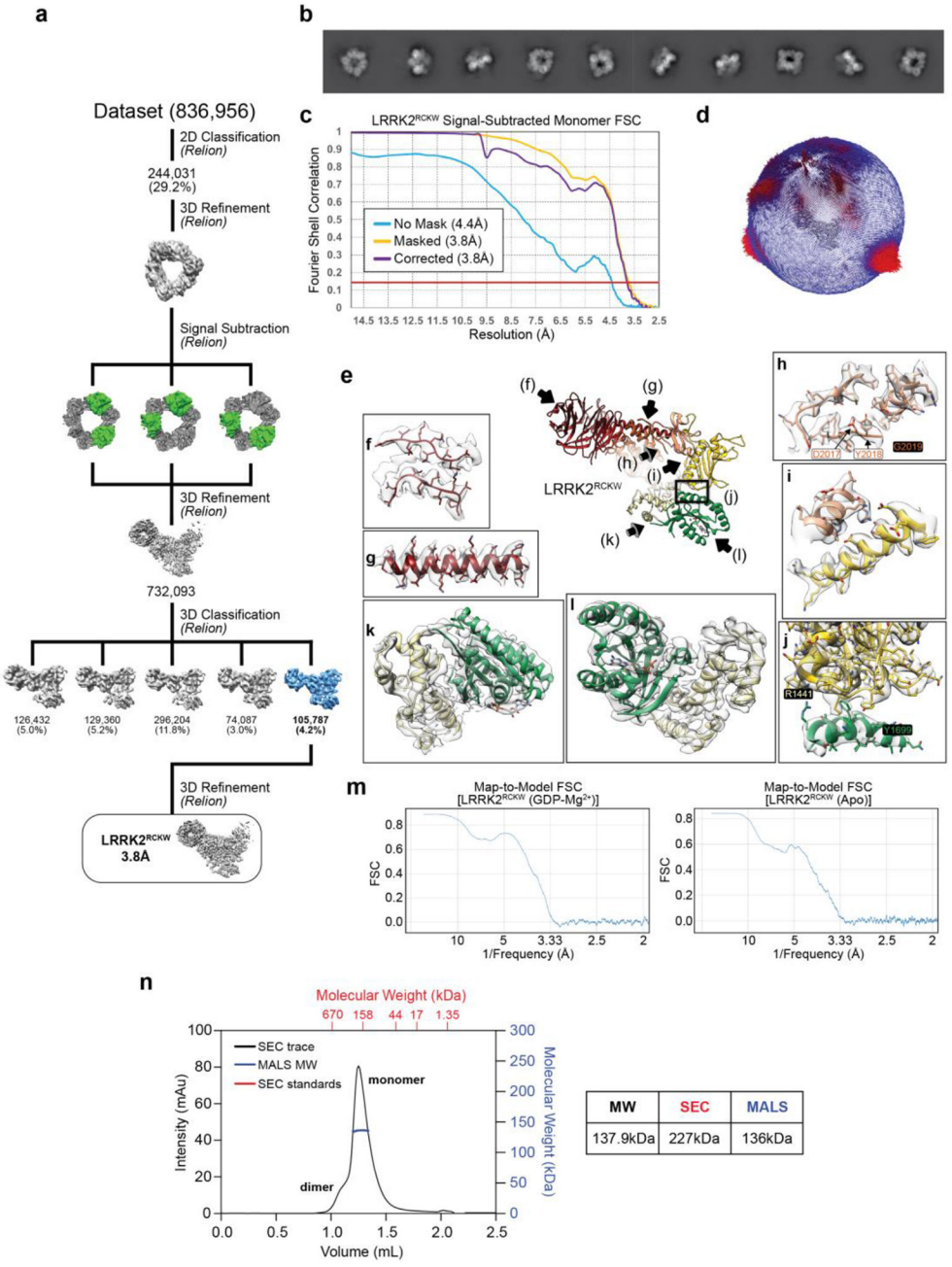

MW	SEC	MALS
137.9kDa	227kDa	136kDa

Extended Data Figure 2 |. Cryo-EM analysis of a signal-subtracted LRRK2^{RCKW} trimer and map-to-model fit.

a, Processing strategy used to obtain a 3.8Å structure of LRRK2^{RCKW} generated from a signal-subtracted trimer where only one monomer contains the RoC and COR-A domains. This structure improved the resolution of the RoC and COR-A domains relative to the full trimer (Extended Data Fig. 1). **b-d**, 2D class averages (b), Fourier Shell Correlations (from Relion) (c), and Euler angle distribution (from Relion) (d) for the 3.8Å-resolution signal-subtracted LRRK2^{RCKW} structure. **e,** Close-ups (f-l) of different parts of the final model fit into the map. **f**, Section of the WD40 domain. **g**, C-terminal helix and its interface with the kinase domain. **h**, Active site of the kinase. Residues in the DYG motif are labeled. G2019,

the site of a major PD-associated mutation (G2019S) and the last residue of the activation loop seen in our structure, is highlighted by a black rounded square. **i**, Interface between COR-B and the αC helix of the N-lobe of the kinase domain. **j**, Interface between the RoC and COR-B domains. R1441 and Y1699, two residues mutated in PD, are labeled. **k, l**, Two different views of the RoC and COR-A domains with GDP-Mg^{2+} modeled into the density. Side chains were omitted in these two panels, corresponding to the lowest-resolution parts of the map. **m**, Map-to-model FSC plots for the top-ranked $LRRK2^{RCKW}$ models, with (left) or without GDP-Mg2+ (right) in the RoC domain. The 0.143 FSC values are reported in Extended Data Table 1. **n**, Size Exclusion Chromatography-Multiple Angle Light Scattering (SEC-MALS) analysis of $LRRK2^{RCKW}$ under the conditions used for cryo-EM (Fig. 1). The table shows the calculated molecular weights (MW) of $LRRK2^{RCKW}$ according to SEC standards (“SEC”) and MALS.

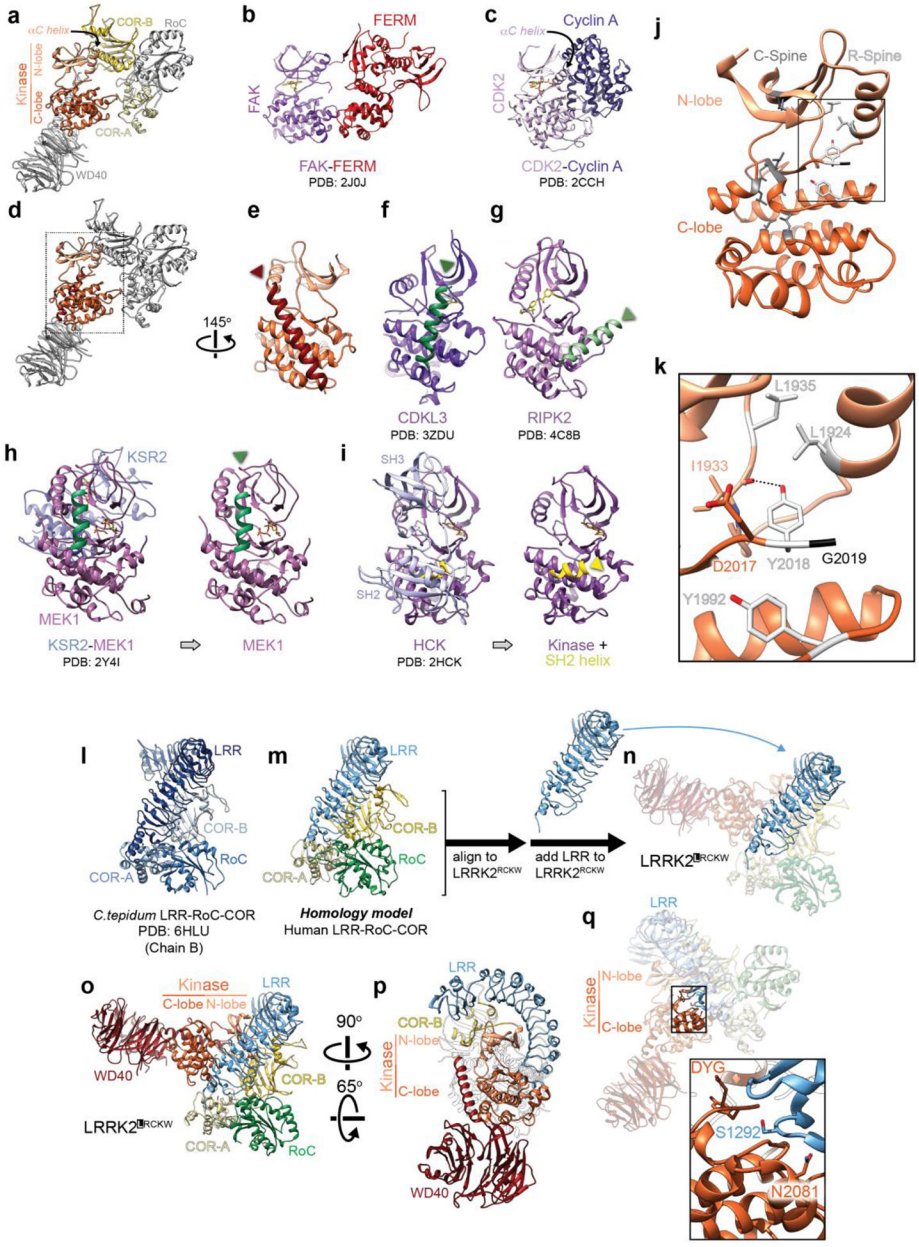

Extended Data Figure 3 |. Comparisons between LRRK2 and other kinases and modelling of the Leucine-Rich Repeat (LRR) into LRRK2^{RCKW}.

a, View of the LRRK2^{RCKW} atomic model with COR-A, COR-B and kinase domains colored. The N- and C-lobes of the kinase are labeled, as is the αC helix in the N-lobe. **b, c,** The FAK-FERM (PDB: 2J0J)[17] (b) and CDK2-Cyclin A (PDB: 2CCH)[19] (c) complexes, shown in the same orientation as the kinase in (a). The αC helix of CDK2 is also labeled. **d,** Same view as in (a) with only the kinase domain and the C-terminal helix colored. **e,** Rotated view of LRRK2's kinase domain with the C-terminal helix facing the viewer. **f, g,** CDKL3 (PDB: 3ZDU) (f) and RIPK2 (PDB: 4C8B)[32] (g) shown in the same orientation as LRRK2's kinase in (e), with alpha helices with the same general location as LRRK2's C-terminal helix colored in green. **h,** KSR2-MEK1 complex (PDB: 2Y4I), with the kinase

oriented as in (e) (left) and after removing KSR2 for clarity (right). The alpha helix associated with the kinase is shown in green. **i,** HCK (PDB: 2HCK) in complex with its SH2 and SH3 domains with the kinase oriented as in (e) (left), and after removal of the SH2 and SH3 domains for clarity (right). A remaining alpha helix from the SH2 domain is shown in yellow. **j,** Front view of LRRK2's kinase with the C-Spine and R-Spine residues colored in grey and white, respectively. **k,** Close-up of the DYG motif and neighboring R-Spine residues. A putative hydrogen bond between Y2018 and the backbone carbonyl of I1933 is shown (O-O distance: 2.7Å). This interaction provides a structural explanation for the hyperactivation of the kinase resulting from a Y2018F mutation[38], which would release the activation loop.

l, Crystal structure of the LRR-RoC-COR(A/B) domains from *C. tepidum* Roco (PDB: 6HLU)[7]. **m**, Homology model for human LRR-RoC-COR(A/B) based on the *C. tepidum* Roco structure (from SWISS-MODEL). **n**, Chimeric model combining $LRRK2^{RCKW}$ and the homology model for the LRR domain from (m) obtained by aligning their RoC-COR(A/B) domains. **o**, **p**, Two views of the hybrid $LRRK2^{LRCKW}$ model. **q**, Close-up showing the proximity between the active site of the kinase (with the side chains of its DYG motif shown) and the S1292 autophosphorylation site on the LRR. The close-up also highlights the proximity between N2081, a residue implicated in Crohn's Disease, and the LRR.

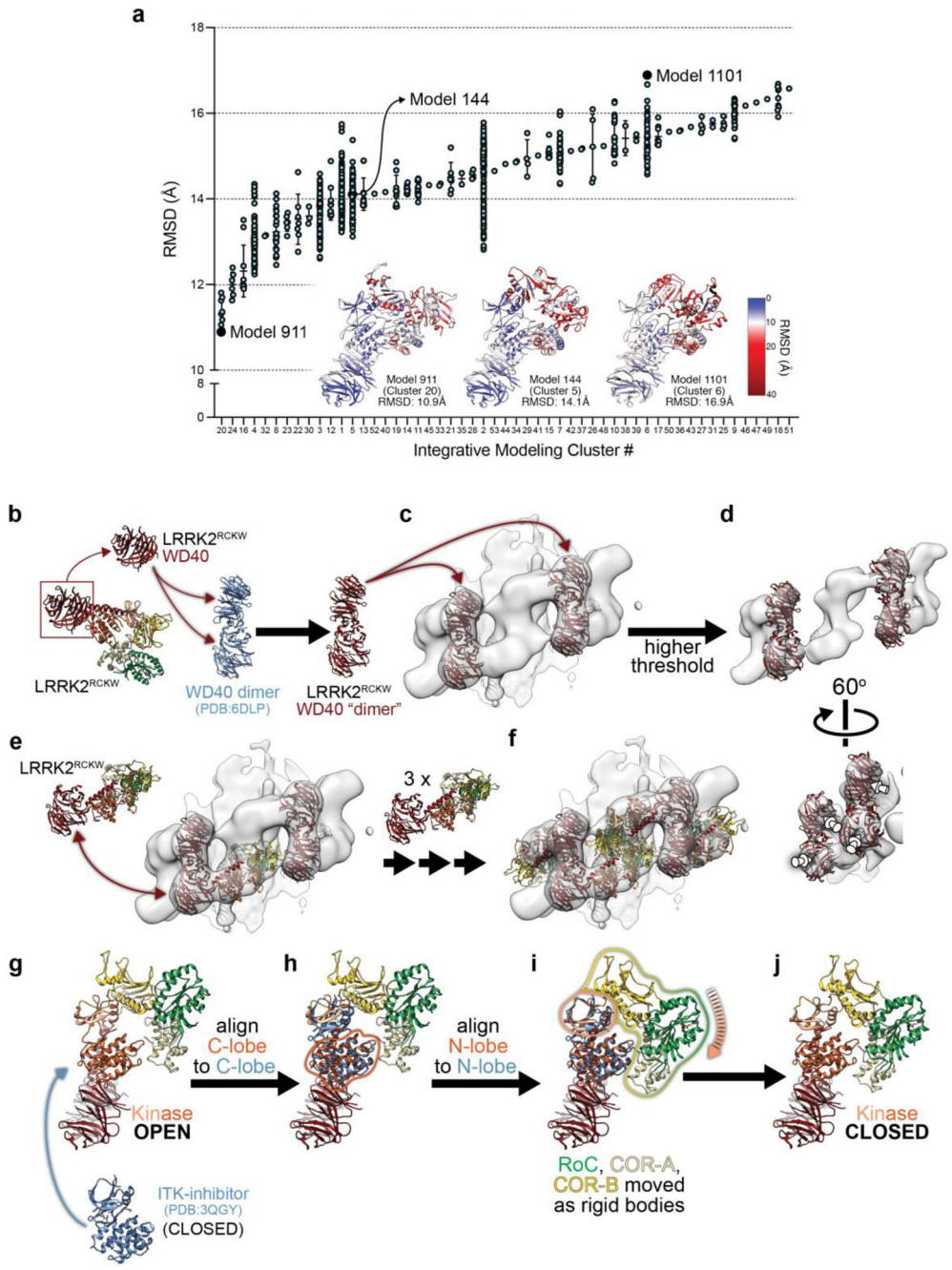

Extended Data Figure 4 |. Comparison between LRRK2^{RCKW} and integrative models built into cryo-ET maps of LRRK2 filaments in cells and docking of LRRK2^{RCKW} into those maps.

a, Root-mean-square deviation (RMSD) between the atomic model of LRRK2^{RCKW} and each of the 1,167 integrative models generated by Watanabe, Buschauer, Bohning and colleagues[5]. RMSDs were calculated in Chimera[45] using 100% residue similarity and with pruning iterations turned off. RMSD values are grouped into 53 clusters of related models (see[5] for details), with the mean and standard deviation shown whenever the cluster contains two or more models. Integrative models that gave the lowest, median and highest RMSD values are shown. The models are colored according to the per-residue RMSD with the

atomic model of LRRK2^{RCKW}. **b**, The WD40s in the crystal structure of a dimer of LRRK2's WD40 (PDB: 6DLP)[9] were replaced with the WD40s from our cryo-EM structure of LRRK2^{RCKW}. **c,** The resulting dimer was fitted into the 14Å cryo-ET map of cellular microtubule-associated LRRK2 filaments[5]. **d,** Two views of the same fitting shown in (c), displayed with a higher threshold for the map to highlight the fitting of the WD40 β-propellers into the density. The white arrows point towards the holes at the center of the β-propellers densities. **e**, Four copies of LRRK2^{RCKW} were docked into the cryo-ET map by aligning their WD40 domains to the docked WD40 dimer. **f**, Model containing the four aligned LRRK2^{RCKW}. **g-j**, Modeling of the kinase-closed form of LRRK2^{RCKW}. **g, h,** The structure of ITK bound to an inhibitor (PDB: 3QGY)[46], which is in a closed conformation, was aligned to LRRK2^{RCKW} using only the C-lobes of the two kinases. **i**, The N-terminal portion of LRRK2^{RCKW}, comprising RoC, COR-A, COR-B and the N-lobe of the kinase, was aligned to ITK using only the N-lobes of the kinases. RoC, COR-A and COR-B were moved as a rigid body in this alignment. **j**, Kinase-closed model of LRRK2^{RCKW}.

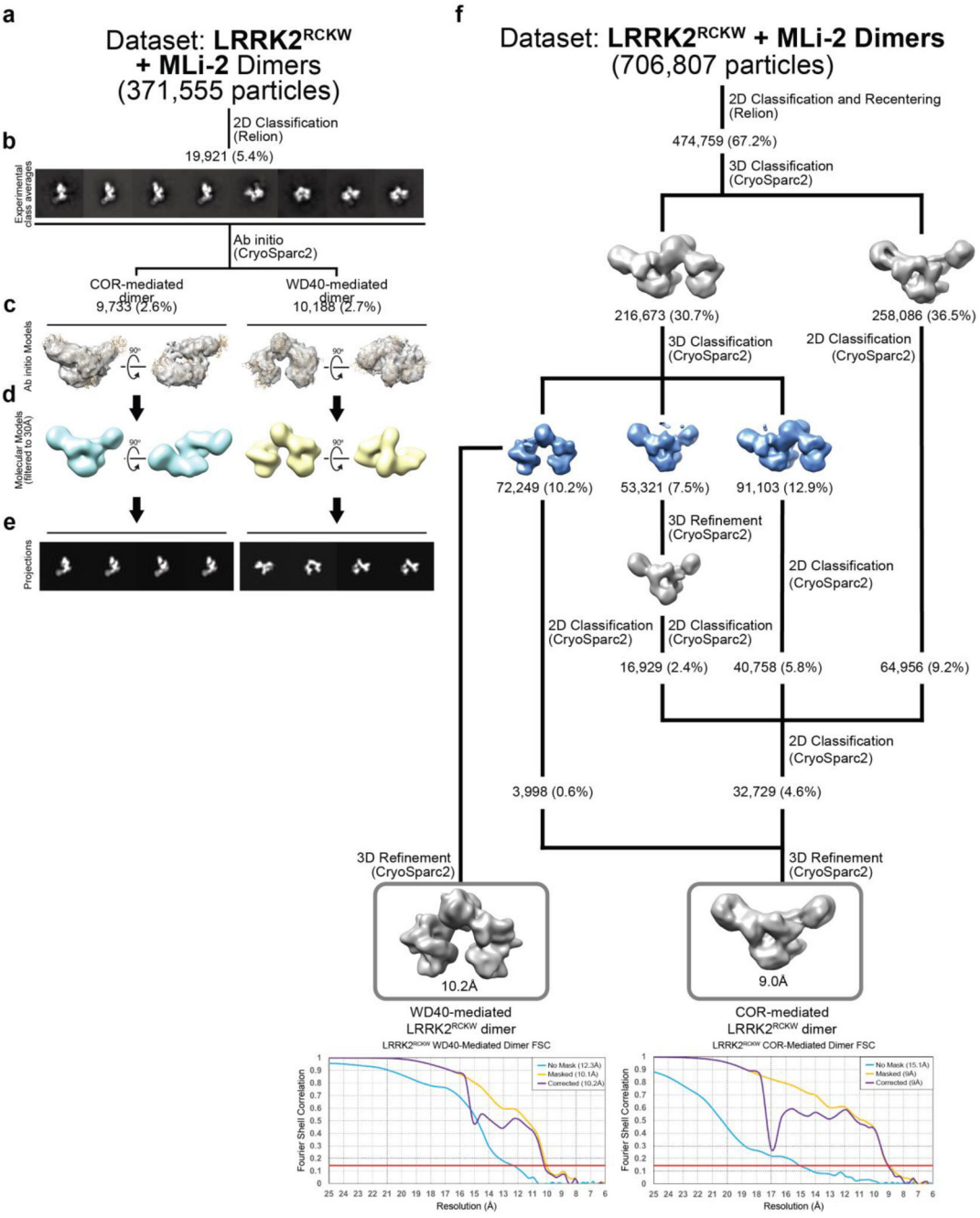

Extended Data Figure 5 | *Ab initio* models for cryo-EM of LRRK2^{RCKW} dimers and cryo-EM analysis of WD40- and COR-mediated dimers of LRRK2^{RCKW} in the presence of the inhibitor MLi-2.

a, An initial dataset was collected from a sample of LRRK2^{RCKW} incubated in the presence of the kinase inhibitor MLi-2 and dimers were selected. **b,** Representative two-dimensional class averages used for *ab initio* model building. **c,** *Ab initio* models with the structure of LRRK2^{RCKW} docked in. **d,** Volumes generated form the molecular models in (b), filtered to 30Å resolution. **e,** Projections of the volumes in (d) shown in the same order as their corresponding 2D class averages in (b). **f**, Data processing strategy for obtaining cryo-EM

structures of WD40- and COR-mediated dimers of LRRK2^{RCKW} in the presence of the inhibitor MLi-2. The models used during this processing (see Methods) are those shown in (d) along with an additional linear trimer (see Methods) used for particle sorting.

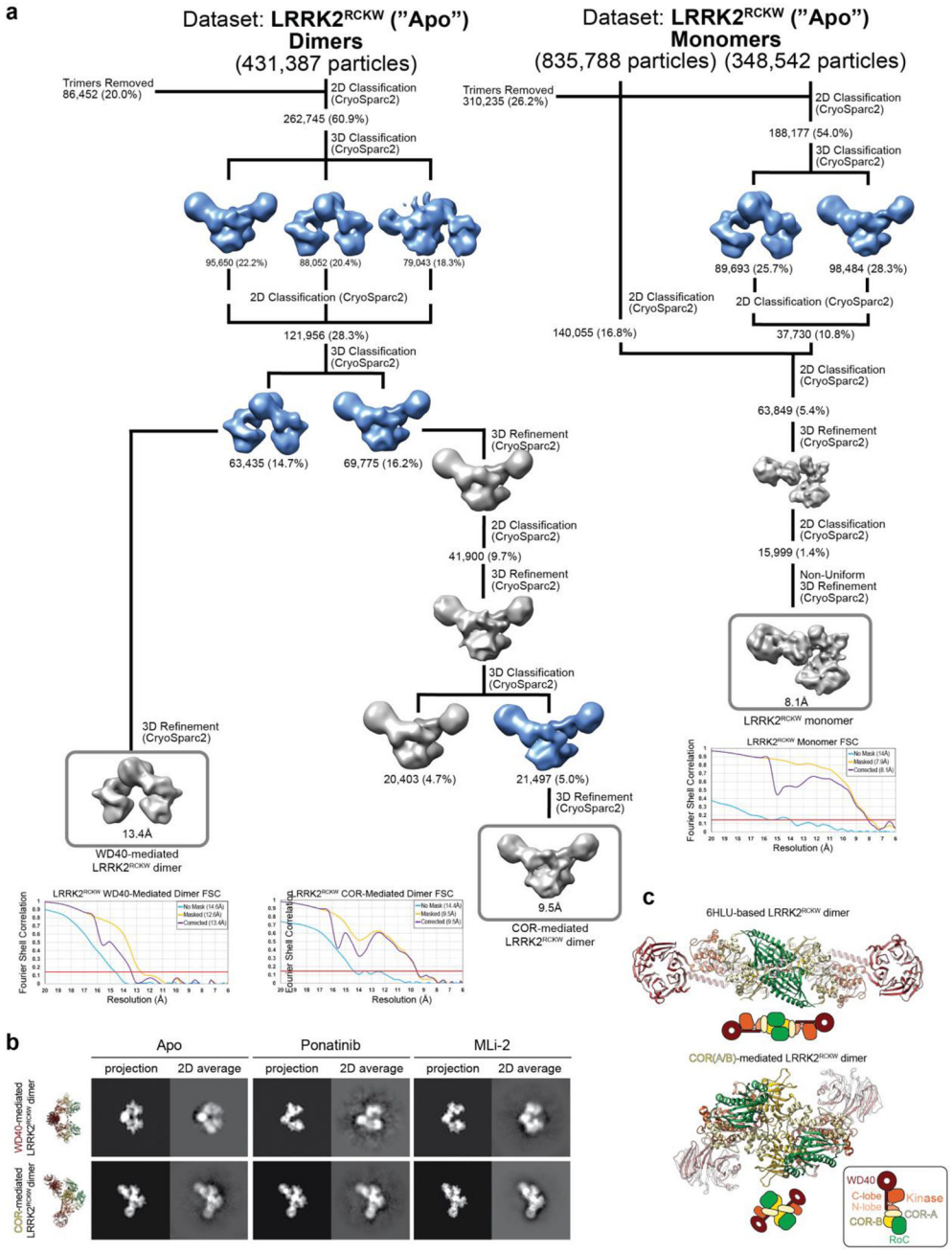

Extended Data Figure 6 |. Cryo-EM analysis of a monomer and WD40- and COR-mediated dimers of LRRK2^{RCKW} in the absence of inhibitor ("Apo") and dimerization of LRRK2^{RCKW} outside the filaments.

a, Data processing strategy for obtaining cryo-EM structures of a monomer and WD40- and COR-mediated dimers of LRRK2^{RCKW} in the absence of inhibitor. The models used during the processing of the dimers (see Methods) are those shown in Extended Data Fig. 5d, along

with an additional linear trimer (see Methods) used for particle sorting. The models used for processing of the monomer (see Methods) were the same dimer models as in Extended Data Fig. 5d (used for particle sorting) in addition to a monomer model generated from our LRRK2^{RCKW} model (used for refinement). **b**, Two-dimensional (2D) class averages of WD40- and COR-mediated LRRK2^{RCKW} dimers obtained in the absence of inhibitors ("Apo") or in the presence of either Ponatinib or MLi-2. The same molecular models of the two dimers shown in Fig. 3 are shown on the left but in orientations similar to those represented by the 2D class averages shown here. For each class average, a projection from the corresponding model in the best-matching orientation is shown to its left. **c**, Two copies of the LRRK2^{RCKW} structure were aligned to the RoC-COR domains of the LRR-RoC-COR structure from *C. tepidum*'s Roco protein (PDB: 6HLU) to replicate the interface observed in the bacterial homolog in the context of the human protein. This panel shows a comparison between the dimer modeled based on the *C. tepidum* LRR-RoC-COR structure and the dimer observed for LRRK2^{RCKW} in this work. While the bacterial structure shows a dimerization interface that involves the GTPase (RoC), LRRK2^{RCKW} interacts exclusively through its COR-A and -B domains, with the RoC domains located away from this interface. The two arrangements are shown schematically in cartoon form below the structures.

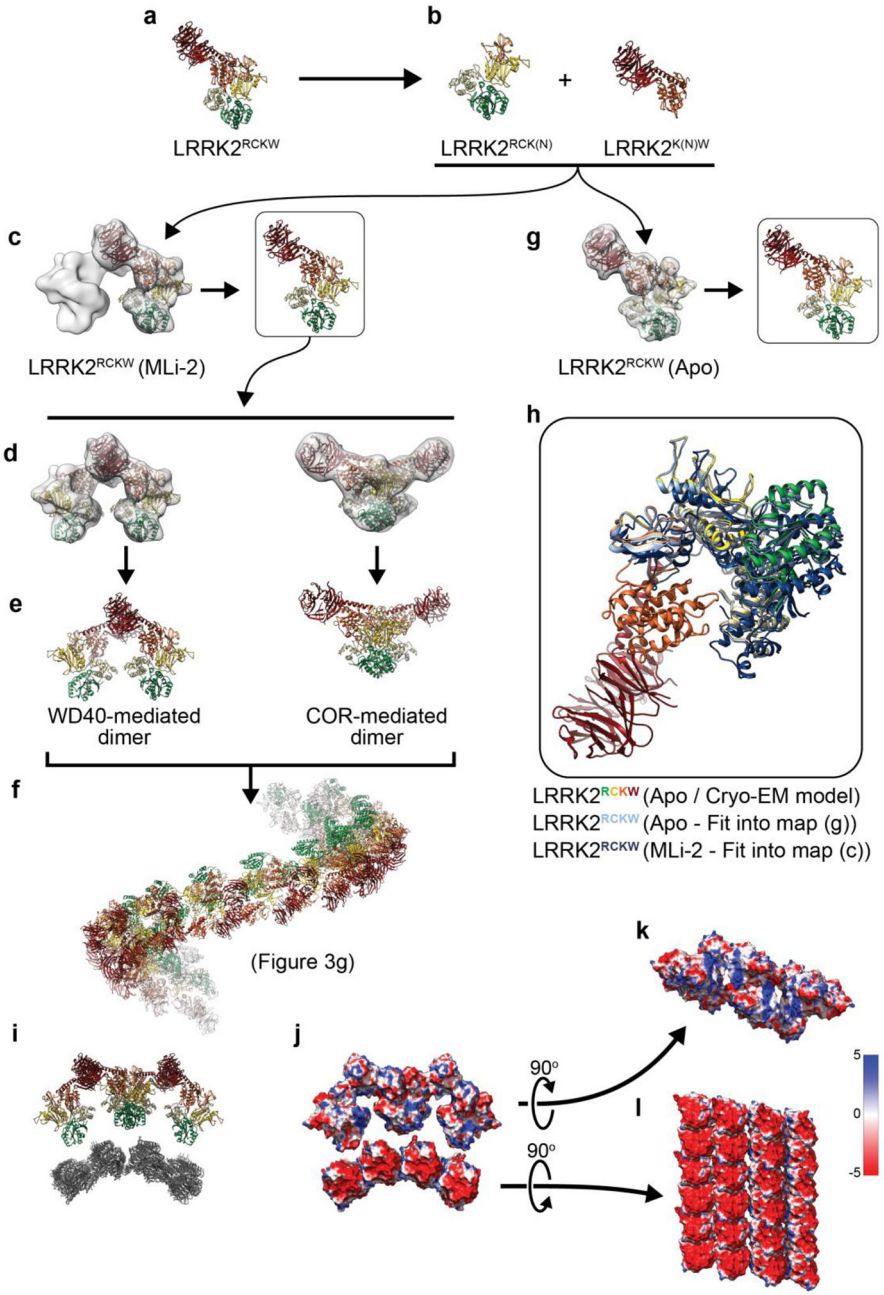

Extended Data Figure 7 | Properties of the microtubule-associated LRRK2^{RCKW} filaments. **a, b,** The LRRK2^{RCKW} structure solved in this work (a) was split at the junction between the N- and C-lobes of the kinase domain (L1949-A1950) (b). **c,** Docking of the two halves of LRRK2^{RCKW} into a cryo-EM map of a LRRK2^{RCKW} dimer solved in the presence of MLi-2. The dimer map is the same one shown in Fig. 3 and Extended Data Figs. 10 and 11. **d,** The model obtained in (c) was docked into cryo-EM maps of either WD40- or COR-mediated dimers obtained in the presence of MLi-2. **e,** Molecular models resulting from the docking in (d). **f**, Aligning, in alternating order, copies of the dimer models generated in (d, e) results in a right-handed filament with dimensions compatible with those of a

microtubule, and its RoC domains pointing inwards (see Fig. 3g-i for more details). **g**, Docking of the two halves of $LRRK2^{RCKW}$ into a cryo-EM map of a $LRRK2^{RCKW}$ monomer solved in the absence of inhibitor ("Apo"). The map is the one shown in Fig. 1h and Extended Data Fig. 6. **h**, Three-way comparison of $LRRK2^{RCKW}$ (with domain colors) and the models resulting from the dockings into the MLi-2 WD40-mediated dimer map (c) (dark blue) and "Apo" monomer map (g) (light blue). The three structures were aligned using the C-lobes of their kinases and the WD40 domain. The superposition illustrates that the docking into the "Apo" map results in a structure very similar to that obtained from the trimer (Fig. 1) and that the presence of MLi-2 leads to a closing of the kinase. **i**, Molecular model of the microtubule-associated $LRRK2^{RCKW}$ filament obtained by docking a fragment of a microtubule structure (PDB: 6O2S) into the corresponding density in the sub-tomogram average (Fig. 2a). **j**, Same view as in (i) with the models shown as surface representations colored by their Coulomb potential. **k, l,** "Peeling off" of the structure shown in (j), with the $LRRK2^{RCKW}$ filament seen from the perspective of the microtubule surface (k) and the microtubule surface seen from the perspective of the $LRRK2^{RCKW}$ filament (l). Note: the acidic C-terminal tubulin tails are not ordered in the microtubule structure and thus are not included in the surface charge distributions. The Coulomb potential coloring scale is shown on the right.

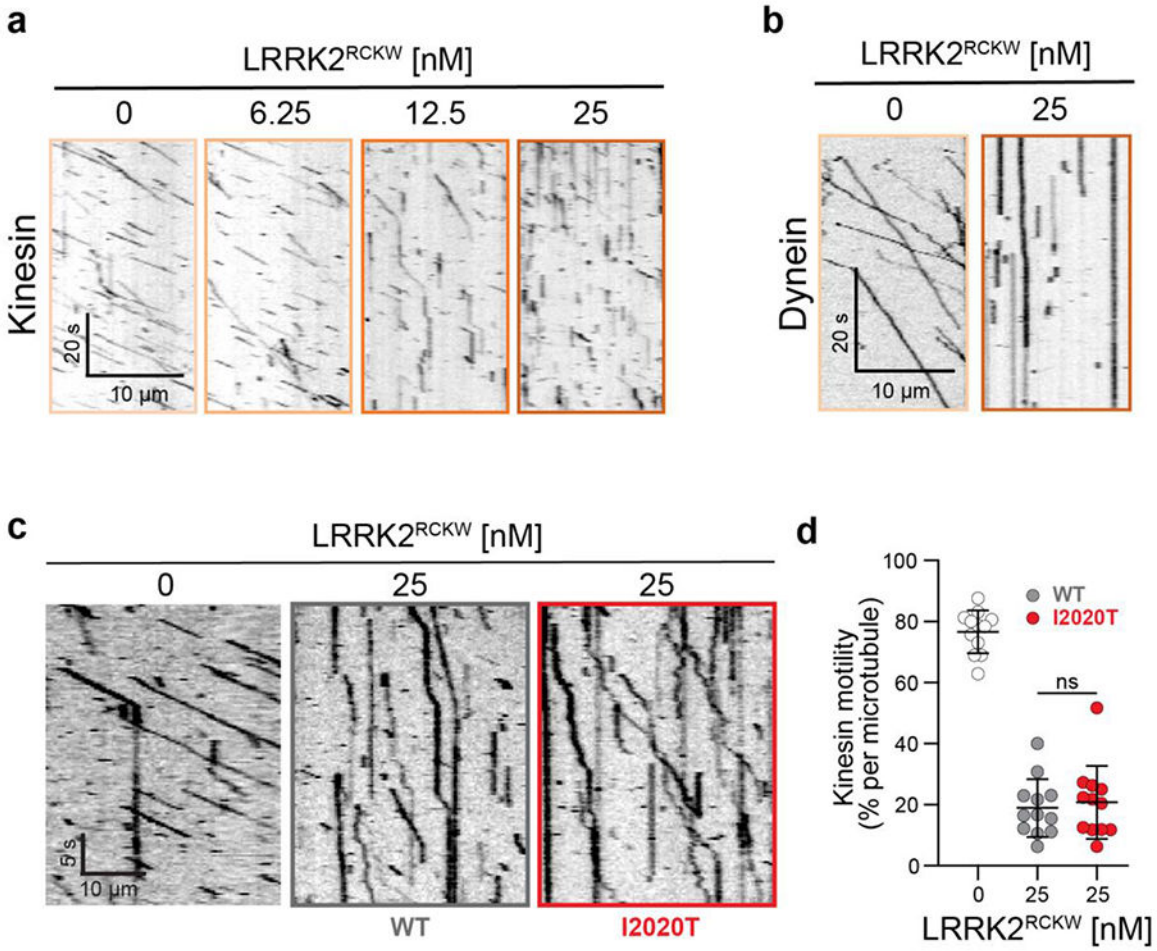

Extended Data Figure 8 |. Inhibition of motor motility by wild-type and I2020T LRRK2^{RCKW}. **a**, Example kymographs showing that increasing concentrations of LRRK2^{RCKW} reduce kinesin runs. **b,** Example kymographs showing that 25 nM LRRK2^{RCKW} reduces dynein runs. **c,** Representative kymographs of kinesin motility in the presence or absence of WT and I2020T LRRK2^{RCKW}. **d**, The percentage of motile kinesin events per microtubule in the absence of LRRK2 or in the presence of 25 nM WT or I2020T LRRK2^{RCKW}. Data are mean ± s.d. (n = 12 microtubules per condition quantified from two independent experiments). There is a significant difference between 0 nM and both 25 nM RCKW conditions ($p < 0.0001$), but no significant (ns) difference between the inhibitory effects of WT LRRK2^{RCKW} versus I2020T LRRK2^{RCKW} as calculated using the Kruskal-Wallis test with Dunn's posthoc for multiple comparisons (compared to no LRRK2^{RCKW}).

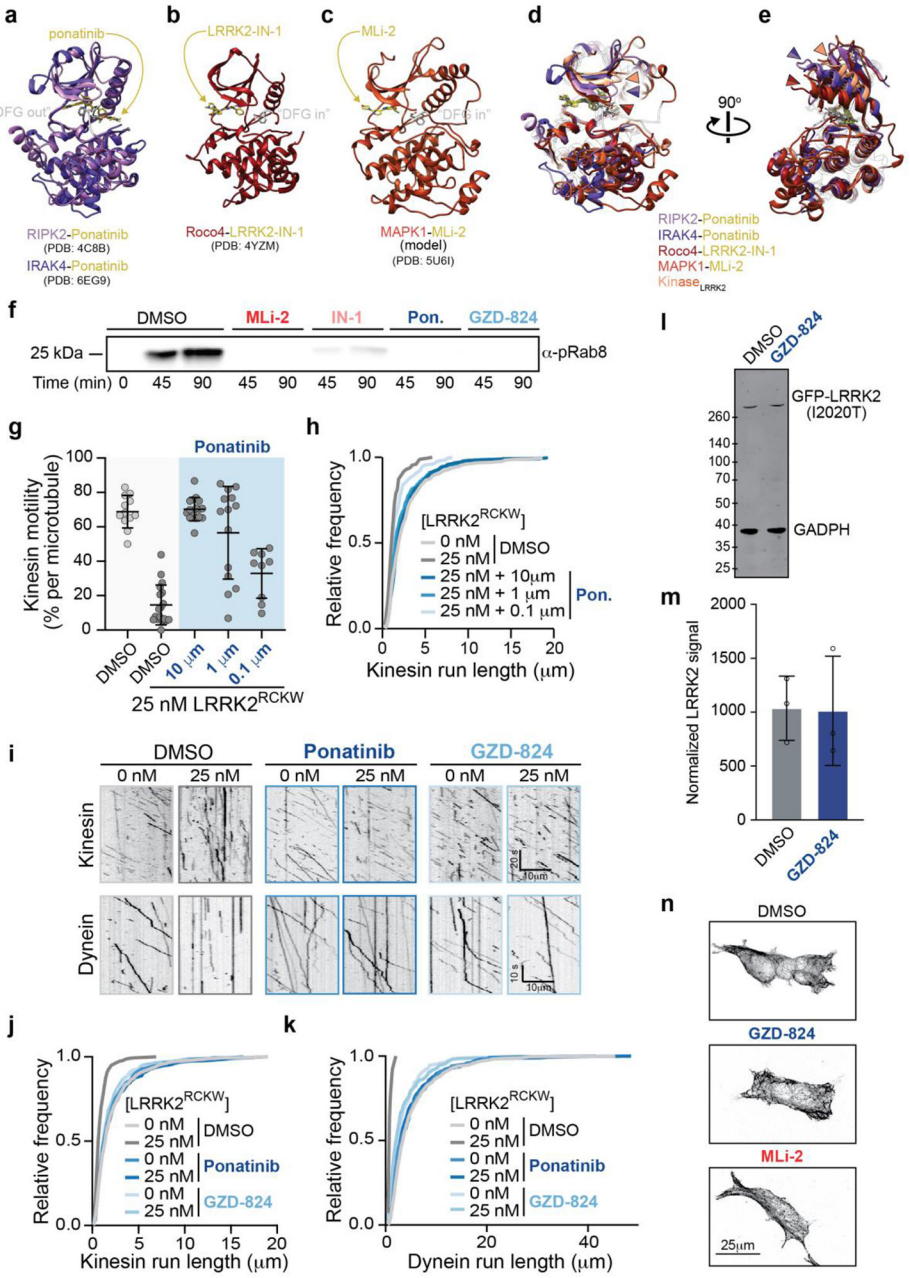

Extended Data Figure 9 |. Type II kinase inhibitors rescue kinesin and dynein motility.

a-e, Ponatinib is a Type II, "DFG out" inhibitor. **a**, Superposition of the structures of Ponatinib-bound RIPK2 (PDB: 4C8B)[32] and IRAK4 (PDB: 6EG9). Ponatinib is shown in yellow, and the DYG motif residues are shown in white. **b**, **c** For comparison, the structures of (a) Roco4 bound to LRRK2-IN-1 (PDB: 4YZM)[35], a LRRK2-specific Type I, "DFG in" inhibitor, and (b) a model of Mitogen-activated kinase 1 (MAPK1) bound to MLi-2 (PDB: 5U6I)[22], another LRRK2-specific Type I, "DFG in" inhibitor are shown. The inhibitor and DFG residues are colored as in (a). **d**, The structures in (a-c), as well as the kinase from $LRRK2^{RCKW}$ are shown superimposed. The color arrowheads point to the N-lobe's β-sheet to highlight the difference in conformation between kinases bound to the two different types

of inhibitors. Note that LRRK2^{RCKW}'s kinase is even more open than the two Ponatinib-bound kinases. **e**, Rotated view of (d), now highlighting the position of the N-lobe's αC helix. An additional alpha helix in the N-lobe of MAPK1 was removed from this view for clarity. **f,** The kinase inhibitors MLi-2 (1 μM), LRRK2-IN-1 (1 μM), Ponatinib (10 μM) and GZD-824 (10 μM) all inhibit LRRK2^{RCKW}'s kinase activity *in vitro* compared to a DMSO control. A western blot using a phospho-specific antibody to Rab8a at the indicated time points is shown. **g,** A dose response curve showing the percentage of motile kinesin events per microtubule as a function of Ponatinib concentration with LRRK2^{RCKW} (25 nM) or without LRRK2^{RCKW}. Data are mean ± s.d. (from left to right: n = 12, 18, 16, 14, and 9 microtubules quantified from one experiment). ****p < 0.0001 (Kruskal-Wallis test with Dunn's posthoc for multiple comparisons, compared to DMSO without LRRK2^{RCKW}). **h,** Dose response curve of run lengths from data in (g) represented as a cumulative frequency distribution. From top to bottom: n = 654, 173, 584, 293, and 129 motile kinesin events. Mean decay constants (tau) ± confidence interval (CI) are (from top to bottom) 2.736 ± 0.113, 1.291 ± 0.181, 2.542 ± 0.124, 2.285 ± 0.134, and 1.653 ± 0.17. **i,** Representative kymographs of kinesin and dynein with DMSO or Type II inhibitors with or without LRRK2^{RCKW}. **j,** The Type II kinase inhibitors Ponatinib and GZD-824 rescue kinesin run length, represented as a cumulative frequency distribution of run lengths with LRRK2^{RCKW} (25 nM) or without LRRK2^{RCKW}. From top to bottom: n = 893, 355, 507, 499, 524, and 529 runs from two independent experiments. Mean decay constants (tau) ± 95% CI are (from top to bottom) 2.070 ± 0.058, 0.8466 ± 0.091, 1.938 ± 0.065, 2.075 ± 0.07, 1.898 ±, 0.065, and 1.718 ± 0.064. Data were resampled with bootstrapping analysis and statistical significance was established using a one-way ANOVA with Dunnett's test for multiple comparisons. DMSO run lengths were significantly different (p < 0.0001) between conditions (0 vs. 25 nM RCKW). Ponatinib (0 vs. 25 nM RCKW) and GZD-824 (0 vs. 25 nM LRRK2) were not significant. **k,** Same as in (j) but with dynein. From top to bottom: n = 659, 28, 289, 306, 254, and 339 runs from two independent experiments. Mean decay constants (tau) ± 95% confidence intervals; microns are 4.980 ± 0.147, 0.846 ± 0.415, 4.686 ± 0.142, 4.445 ± 0.172, 3.156 ± 0.09, 3.432 ± 0.188 (from top to bottom). Statistical significance as in (j) and run lengths were significantly different (p < 0.0001) between DMSO conditions (0 vs. 25 nM RCKW), and not significant for Ponatinib or GZD0824 conditions. The DMSO conditions are reproduced from Fig. 4f for comparison. **l,** Expression levels of GFP-LRRK2 (I2020T) in 293T cells treated with either DMSO or GZD-824 (5 μM). An Immunoblot with anti-GFP (LRRK2) and anti-GADPH (loading control), which is a representative image from three replicates, is shown. **m,** Quantification of GFP-LRRK2 (I2020T) expression levels from western blots similar to (l). Data are mean ± s.d. (n = 3 per condition). GZD-824 is not significantly different from the DMSO-treated control (Mann-Whitney test). **n,** 293T cells immunostained for tubulin showing that the microtubule architecture is not affected by GZD-824 or MLi-2 compared to DMSO treatment.

Extended Data Table 1 | Cryo-EM data collection and model refinement statistics.

The model refinement statistics are reported for four different types of models, two including GDP-Mg^{2+} in the RoC domain and two excluding it. In each case, we report statistics for two types of model: "Monomer w/interfaces" consists of a $LRRK2^{RCKW}$ monomer plus fragments from the neighboring monomers in the C3 trimer that were used during model building and refinement; "Top 10 Monomers" are the top-10 results from Rosetta Relax with the neighboring fragments removed after processing in Rosetta. PDB accession numbers for the models and the EMD code of the maps used for model-building and refinement are indicated. EMD-21250 contains both the C3 map of the $LRRK2^{RCKW}$ trimer used to build the COR-B, kinase and WD40 domains and the signal-subtracted monomer used to build the RoC and COR-A domains. The final models reported here were refined into the signal-subtracted monomer map. (See Methods for details.)

	Trimer	**Monomer (Apo)**	**Dimers (Apo)**	**Dimers (Mli-2)**
	Dataset	**Dataset**	**Dataset**	**Dataset**
Data Collection				
Number of grids used	1	10	3	2
Microscope	Titan Krios	Talos Arctica	Talos Arctica	Talos Arctica
Camera	Gatan K2	Gatan K2	Gatan K2	Gatan K2
Camera Mode (Counting/Super-Res.)	C	C/SR	C/SR	C
Voltage (kV)	300	200	200	200
Magnification	130,000	36,000	36,000	36,000
Pixel size (Å/pixel)	1.07	1.16/0.58	1.16/0.58	1.16
Dose rate (e^-/Å^2 second)	6.65	4.2-10	4.6-7.8	5.5
Exposure time (s)	8	6-12	7-11	9-10
Total dose (e^-/Å^2)	53.2	50.4-60	50.6-54.6	49.5-55
Number of frames	40	30-60	35-55	45-50
Defocus range (μm)	1-1.8	1-2	1-2	1-2
Micrographs collected (no.)	3,824	11,354	5,303	4,139
Initial particle number	836,956	1,184,330	431,387	706,807
Final particle number	70,954*/105,787#	15,999	63,435[a]/21,497[b]	72,249[a]/36,727[b]
Final Resolution (0.143 FSC threshold) (Å)	3.5*/3.8*	8.1	13.4[a]/9.5[b]	10.2[a]/9.0[b]
$LRRK2^{RCKW}$ Models	**(without GDP-Mg^{2+})**		**(with GDP-Mg^{2+})**	
	Monomer w/interfaces	**Top 10 Monomers****	**Monomer w/interfaces**	**Top 10 Monomers****
	PDB: 6VP8 EMD-21250	**PDB: 6VP7 EMD-21250**	**PDB: 6VP6 EMD-21250**	**PDB: 6VNO EMD-21250**
Model Refinement				
Map-to-model resolution (0.143 FSC threshold) (Å)	3.98	3.98	3.98	3.98
Map B-factor (Å^2)	−136	−136	−136	−136

	Trimer Dataset	Monomer (Apo) Dataset	Dimers (Apo) Dataset	Dimers (Mli-2) Dataset
Model Composition				
Non-hydrogen atoms	13,161	8,534	13,161	8,534
Protein Residues	1,668	1,084	1,668	1,084
Ligands	0	0	1	1
B-factors (Å^2)				
Protein	42.75	49.76	45.49	50.4
Ligand	-	-	193.78	193.78
R.M.S. Deviations				
Bond length (Å)	0.013	0.013	0.090	0.112
Bond angle (°)	1.374	1.384	2.238	2.596
Validation				
Molprobity score	1.37	1.48	1.42	1.51
Clash score	1.69	2.35	2.03	2.61
Poor rotamers (%)	0,00	0.00	0.00	0.00
Ramachandran				
Favored (%)	92.90	92.58	93.02	92.57
Allowed (%)	5.99	6.36	5.99	6.32
Disfavored (%)	1.11	1.06	0.99	1.11

*C3 reconstruction.

#signal-subtracted monomer.

aWD40-mediated dimer.

bCOR-mediated dimer.

**Numbers represent the average of the values for all 10 models.

Supplementary Material

Refer to Web version on PubMed Central for supplementary material.

ACKNOWLEDGEMENTS

We thank Susan Taylor for her role in initiating this collaborative work, which was partially supported by multi-investigator grants from the Michael J Fox Foundation: grant #s: 11425 and 11425.02 (PI: Susan Taylor) and 18321 (PIs: AEL and SLR-P). We also thank the UC San Diego Cryo-EM Facility, the Nikon Imaging Center at UC San Diego, where the confocal microscopy was performed, the use of instruments at the Electron Imaging Center for NanoMachines supported by NIH (1S10RR23057, 1S10OD018111, and 1U24GM116792), NSF (DBI-1338135) and CNSI at UCLA, John P. Gillies and Agnieszka Kendrick for technical support with protein purifications, and Andrea Dickey for feedback on the manuscript. CKD was initially supported by the Molecular Biophysics Training Grant (NIH Grant T32 GM008326) and subsequently by a Predoctoral Fellowship from the Visible Molecular Cell Consortium and Center for Trans-scale Structural Biology (UC San Diego). DS is supported by an A.P. Giannini Foundation postdoctoral fellowship. AKS receives salary and support from the Ludwig Institute for Cancer Research. EV is supported by a NIH Director's New Innovator Award DP2GM123494. SLR-P is an investigator of the Howard Hughes Medical institute and is also supported by R01GM121772. AEL is supported by R01GM107214. SK is grateful for support from the SGC, a registered charity that receives funds from AbbVie, Bayer Pharma AG, Boehringer Ingelheim, Canada Foundation for Innovation, Eshelman Institute for Innovation, Genome Canada, Innovative Medicines Initiative EUbOPEN (agreement No 875510), Janssen, Merck KGaA, MSD, Ontario Ministry of Economic Development and Innovation, Pfizer, São Paulo Research Foundation-FAPESP, Takeda, and the Wellcome, as well as Boehringer Ingelheim for funding initial structural studies of this project.

DATA AVAILABILITY

All reagents and data will be made available upon request. Model coordinates for the LRRK2^{RCKW} structure are deposited in the Protein Data Bank (PDB) as follows: (1) PDB accession code 6VP6: LRRK2^{RCKW} with the adjacent COR-B and WD40 domains (from the trimer) used to optimize residues at those interfaces during refinement in Rosetta, with GDP-Mg^{2+} bound; (2) PDB accession code 6VNO: The top 10 models for LRRK2^{RCKW} without adjacent domains, with GDP-Mg^{2+} bound; (3) PDB accession code 6VP8: LRRK2^{RCKW} with the adjacent COR-B and WD40 domains (from the trimer) used to optimize residues at those interfaces during refinement in Rosetta, no GDP-Mg^{2+}; (4) PDB accession code 6VP7: The top 10 models for LRRK2^{RCKW} without adjacent domains, no GDP-Mg^{2+} bound. Cryo-EM maps for the different LRRK2^{RCKW} structures are deposited at the EMDB as follows: (1) EMD accession code 21250: This deposition contains both the 3.5Å map of LRRK2^{RCKW} trimer (used to build the COR-B, kinase and WD40 domains) and the 3.8Å map of the signal-subtracted LRRK2^{RCKW} trimer (used to build the RoC and COR-A domains); (2) EMD accession code 21306: 8.1Å map of LRRK2^{RCKW} monomer; (3) EMD accession code 21309: 9.5Å map of COR-mediated LRRK2^{RCKW} dimer in the absence of kinase ligand (“apo”); (4) EMD accession code 21310: 13.4Å map of WD40-mediated LRRK2^{RCKW} dimer in the absence of kinase ligand (“apo”); (5) EMD accession code 21311: 9.0Å map of COR-mediated LRRK2^{RCKW} dimer in the presence of MLi-2; (6) EMD accession code 21312: 10.2Å map of WD40-mediated LRRK2^{RCKW} dimer in the presence of MLi-2. Source data for EDF10 are provided with the paper. All other data that support the findings of this study are available from the corresponding authors upon reasonable request.

REFERENCES

1. Monfrini E & Di Fonzo A Leucine-Rich Repeat Kinase (LRRK2) Genetics and Parkinson’s Disease. Adv Neurobiol 14, 3–30 (2017). [PubMed: 28353276]
2. Di Maio R, Hoffman EK, Rocha EM, Keeney MT, Sanders LH, De Miranda BR, Zharikov A, Van Laar A, Stepan AF, Lanz TA, Kofler JK, Burton EA, Alessi DR, Hastings TG & Greenamyre JT LRRK2 activation in idiopathic Parkinson’s disease. Sci Transl Med 10, (2018).
3. Abeliovich A & Gitler AD Defects in trafficking bridge Parkinson’s disease pathology and genetics. Nature 539, 207–216 (2016). [PubMed: 27830778]
4. Gloeckner CJ, Kinkl N, Schumacher A, Braun RJ, O’Neill E, Meitinger T, Kolch W, Prokisch H & Ueffing M The Parkinson disease causing LRRK2 mutation I2020T is associated with increased kinase activity. Hum Mol Genet 15, 223–232 (2006). [PubMed: 16321986]
5. Watanabe R, Buschauer R, Bohning J, Audagnotto M, Lasker K, Lu TW, Boassa D, Taylor S & Villa E The in situstructure of Parkinson’s disease-linked LRRK2. bioRxiv 7, (2019).
6. Gotthardt K, Weyand M, Kortholt A, Van Haastert PJM & Wittinghofer A Structure of the Roc-COR domain tandem of C. tepidum, a prokaryotic homologue of the human LRRK2 Parkinson kinase. EMBO J 27, 2239–2249 (2008). [PubMed: 18650931]
7. Deyaert E, Leemans M, Singh RK, Gallardo R, Steyaert J, Kortholt A, Lauer J & Versées W Structure and nucleotide-induced conformational dynamics of the Chlorobium tepidum Roco protein. Biochem J 476, 51–66 (2019). [PubMed: 30538153]
8. Deng J, Lewis PA, Greggio E, Sluch E, Beilina A & Cookson MR Structure of the ROC domain from the Parkinson’s disease-associated leucine-rich repeat kinase 2 reveals a dimeric GTPase. Proc Natl Acad Sci USA 105, 1499–1504 (2008). [PubMed: 18230735]

9. Zhang P, Fan Y, Ru H, Wang L, Magupalli VG, Taylor SS, Alessi DR & Wu H Crystal structure of the WD40 domain dimer of LRRK2. Proc Natl Acad Sci USA 116, 1579–1584 (2019). [PubMed: 30635421]

10. Guaitoli G, Raimondi F, Gilsbach BK, Gómez-Llorente Y, Deyaert E, Renzi F, Li X, Schaffner A, Jagtap PKA, Boldt K, von Zweydorf F, Gotthardt K, Lorimer DD, Yue Z, Burgin A, Janjic N, Sattler M, Versées W, Ueffing M, Ubarretxena-Belandia I, Kortholt A & Gloeckner CJ Structural model of the dimeric Parkinson's protein LRRK2 reveals a compact architecture involving distant interdomain contacts. Proc Natl Acad Sci USA 113, 4357–66 (2016).

11. Sejwal K, Chami M, Rémigy H, Vancraenenbroeck R, Sibran W, Sütterlin R, Baumgartner P, McLeod R, Chartier-Harlin M-C, Baekelandt V, Stahlberg H & Taymans J-M Cryo-EM analysis of homodimeric full-length LRRK2 and LRRK1 protein complexes. Sci Rep 7, 8667 (2017). [PubMed: 28819229]

12. Kett LR, Boassa D, Ho CC-Y, Rideout HJ, Hu J, Terada M, Ellisman M & Dauer WT LRRK2 Parkinson disease mutations enhance its microtubule association. Hum Mol Genet 21, 890–899 (2012). [PubMed: 22080837]

13. Steger M, Tonelli F, Ito G, Davies P, Trost M, Vetter M, Wachter S, Lorentzen E, Duddy G, Wilson S, Baptista MA, Fiske BK, Fell MJ, Morrow JA, Reith AD, Alessi DR & Mann M Phosphoproteomics reveals that Parkinson's disease kinase LRRK2 regulates a subset of Rab GTPases. eLife 5, e12813 (2016). [PubMed: 26824392]

14. Steger M, Diez F, Dhekne HS, Lis P, Nirujogi RS, Karayel O, Tonelli F, Martinez TN, Lorentzen E, Pfeffer SR, Alessi DR & Mann M Systematic proteomic analysis of LRRK2-mediated Rab GTPase phosphorylation establishes a connection to ciliogenesis. eLife 6, e31012 (2017). [PubMed: 29125462]

15. Ito G, Okai T, Fujino G, Takeda K, Ichijo H, Katada T & Iwatsubo T GTP binding is essential to the protein kinase activity of LRRK2, a causative gene product for familial Parkinson's disease. Biochemistry 46, 1380–1388 (2007). [PubMed: 17260967]

16. West AB, Moore DJ, Choi C, Andrabi SA, Li X, Dikeman D, Biskup S, Zhang Z, Lim K-L, Dawson VL & Dawson TM Parkinson's disease-associated mutations in LRRK2 link enhanced GTP-binding and kinase activities to neuronal toxicity. Hum Mol Genet 16, 223–232 (2007). [PubMed: 17200152]

17. Lietha D, Cai X, Ceccarelli DFJ, Li Y, Schaller MD & Eck MJ Structural basis for the autoinhibition of focal adhesion kinase. Cell 129, 1177–1187 (2007). [PubMed: 17574028]

18. Terheyden S, Ho FY, Gilsbach BK, Wittinghofer A & Kortholt A Revisiting the Roco G-protein cycle. Biochem J 465, 139–147 (2015). [PubMed: 25317655]

19. Cheng K-Y, Noble MEM, Skamnaki V, Brown NR, Lowe ED, Kontogiannis L, Shen K, Cole PA, Siligardi G & Johnson LN The role of the phospho-CDK2/cyclin A recruitment site in substrate recognition. J Biol Chem 281, 23167–23179 (2006). [PubMed: 16707497]

20. Pungaliya PP, Bai Y, Lipinski K, Anand VS, Sen S, Brown EL, Bates B, Reinhart PH, West AB, Hirst WD & Braithwaite SP Identification and characterization of a leucine-rich repeat kinase 2 (LRRK2) consensus phosphorylation motif. PLoS ONE 5, e13672 (2010). [PubMed: 21060682]

21. Hui KY, Fernandez-Hernandez H, Hu J, Schaffner A, Pankratz N, Hsu N-Y, Chuang L-S, Carmi S, Villaverde N, Li X, Rivas M, Levine AP, Bao X, Labrias PR, Haritunians T, Ruane D, Gettler K, Chen E, Li D, Schiff ER, Pontikos N, Barzilai N, Brant SR, Bressman S, Cheifetz AS, Clark LN, Daly MJ, Desnick RJ, Duerr RH, Katz S, Lencz T, Myers RH, Ostrer H, Ozelius L, Payami H, Peter Y, Rioux JD, Segal AW, Scott WK, Silverberg MS, Vance JM, Ubarretxena-Belandia I, Foroud T, Atzmon G, Pe'er I, Ioannou Y, McGovern DPB, Yue Z, Schadt EE, Cho JH & Peter I Functional variants in the LRRK2 gene confer shared effects on risk for Crohn's disease and Parkinson's disease. Sci Transl Med 10, eaai7795 (2018). [PubMed: 29321258]

22. Scott JD, DeMong DE, Greshock TJ, Basu K, Dai X, Harris J, Hruza A, Li SW, Lin S-I, Liu H, Macala MK, Hu Z, Mei H, Zhang H, Walsh P, Poirier M, Shi Z-C, Xiao L, Agnihotri G, Baptista MAS, Columbus J, Fell MJ, Hyde LA, Kuvelkar R, Lin Y, Mirescu C, Morrow JA, Yin Z, Zhang X, Zhou X, Chang RK, Embrey MW, Sanders JM, Tiscia HE, Drolet RE, Kern JT, Sur SM, Renger JJ, Bilodeau MT, Kennedy ME, Parker EM, Stamford AW, Nargund R, McCauley JA & Miller MW Discovery of a 3-(4-Pyrimidinyl) Indazole (MLi-2), an Orally Available and Selective

Leucine-Rich Repeat Kinase 2 (LRRK2) Inhibitor that Reduces Brain Kinase Activity. J Med Chem 60, 2983–2992 (2017). [PubMed: 28245354]

23. Fell MJ, Mirescu C, Basu K, Cheewatrakoolpong B, DeMong DE, Ellis JM, Hyde LA, Lin Y, Markgraf CG, Mei H, Miller M, Poulet FM, Scott JD, Smith MD, Yin Z, Zhou X, Parker EM, Kennedy ME & Morrow JA MLi-2, a Potent, Selective, and Centrally Active Compound for Exploring the Therapeutic Potential and Safety of LRRK2 Kinase Inhibition. J Pharmacol Exp Ther 355, 397–409 (2015). [PubMed: 26407721]
24. Case RB, Pierce DW, Hom-Booher N, Hart CL & Vale RD The directional preference of kinesin motors is specified by an element outside of the motor catalytic domain. Cell 90, 959–966 (1997). [PubMed: 9298907]
25. Redwine WB, DeSantis ME, Hollyer I, Htet ZM, Tran PT, Swanson SK, Florens L, Washburn MP & Reck-Peterson SL The human cytoplasmic dynein interactome reveals novel activators of motility. eLife 6, e28257 (2017). [PubMed: 28718761]
26. Dixit R, Ross JL, Goldman YE & Holzbaur ELF Differential regulation of dynein and kinesin motor proteins by tau. Science (New York, N.Y.) 319, 1086–1089 (2008).
27. Monroy BY, Tan TC, Oclaman JM, Han JS, Simó S, Niwa S, Nowakowski DW, McKenney RJ & Ori-McKenney KM A Combinatorial MAP Code Dictates Polarized Microtubule Transport. Dev Cell 53, 60–72.e4 (2020). [PubMed: 32109385]
28. Reck-Peterson S, Yildiz A, Carter A, Gennerich A, Zhang N & Vale R Single-molecule analysis of dynein processivity and stepping behavior. Cell 126, 335–348 (2006). [PubMed: 16873064]
29. Qiu W, Derr ND, Goodman BS, Villa E, Wu D, Shih W & Reck-Peterson SL Dynein achieves processive motion using both stochastic and coordinated stepping. Nat Struct Mol Biol 19, 193–200 (2012). [PubMed: 22231401]
30. DeWitt MA, Chang AY, Combs PA & Yildiz A Cytoplasmic dynein moves through uncoordinated stepping of the AAA+ ring domains. Science (New York, N.Y.) 335, 221–225 (2012).
31. Liu M, Bender SA, Cuny GD, Sherman W, Glicksman M & Ray SS Type II kinase inhibitors show an unexpected inhibition mode against Parkinson's disease-linked LRRK2 mutant G2019S. Biochemistry 52, 1725–1736 (2013). [PubMed: 23379419]
32. Canning P, Ruan Q, Schwerd T, Hrdinka M, Maki JL, Saleh D, Suebsuwong C, Ray S, Brennan PE, Cuny GD, Uhlig HH, Gyrd-Hansen M, Degterev A & Bullock AN Inflammatory Signaling by NOD-RIPK2 Is Inhibited by Clinically Relevant Type II Kinase Inhibitors. Chemistry & biology 22, 1174–1184 (2015). [PubMed: 26320862]
33. Ren X, Pan X, Zhang Z, Wang D, Lu X, Li Y, Wen D, Long H, Luo J, Feng Y, Zhuang X, Zhang F, Liu J, Leng F, Lang X, Bai Y, She M, Tu Z, Pan J & Ding K Identification of GZD824 as an orally bioavailable inhibitor that targets phosphorylated and nonphosphorylated breakpoint cluster region-Abelson (Bcr-Abl) kinase and overcomes clinically acquired mutation-induced resistance against imatinib. J Med Chem 56, 879–894 (2013). [PubMed: 23301703]
34. Deng X, Dzamko N, Prescott A, Davies P, Liu Q, Yang Q, Lee J-D, Patricelli MP, Nomanbhoy TK, Alessi DR & Gray NS Characterization of a selective inhibitor of the Parkinson's disease kinase LRRK2. Nat Chem Biol 7, 203–205 (2011). [PubMed: 21378983]
35. Gilsbach BK, Messias AC, Ito G, Sattler M, Alessi DR, Wittinghofer A & Kortholt A Structural Characterization of LRRK2 Inhibitors. J Med Chem 58, 3751–3756 (2015). [PubMed: 25897865]
36. Godena VK, Brookes-Hocking N, Moller A, Shaw G, Oswald M, Sancho RM, Miller CCJ, Whitworth AJ & De Vos KJ Increasing microtubule acetylation rescues axonal transport and locomotor deficits caused by LRRK2 Roc-COR domain mutations. Nat Commun 5, (2014).
37. Blanca Ramírez M, Lara Ordóñez AJ, Fdez E, Madero-Pérez J, Gonnelli A, Drouyer M, Chartier-Harlin M-C, Taymans J-M, Bubacco L, Greggio E & Hilfiker S GTP binding regulates cellular localization of Parkinson's disease-associated LRRK2. Hum Mol Genet 26, 2747–2767 (2017). [PubMed: 28453723]
38. Schmidt SH, Knape MJ, Boassa D, Mumdey N, Kornev AP, Ellisman MH, Taylor SS & Herberg FW The dynamic switch mechanism that leads to activation of LRRK2 is embedded in the DFGψ motif in the kinase domain. Proc Natl Acad Sci USA 116, 14979–14988 (2019). [PubMed: 31292254]

39. Wang Y, Huynh W, Skokan TD, Lu W, Weiss A & Vale RD CRACR2a is a calcium-activated dynein adaptor protein that regulates endocytic traffic. J Cell Biol 218, 1619–1633 (2019). [PubMed: 30814157]

40. Etoh K & Fukuda M Rab10 regulates tubular endosome formation through KIF13A and KIF13B motors. J Cell Sci 132, (2019).

41. Horgan CP, Hanscom SR, Jolly RS, Futter CE & McCaffrey MW Rab11-FIP3 links the Rab11 GTPase and cytoplasmic dynein to mediate transport to the endosomal-recycling compartment. J Cell Sci 123, 181–191 (2010). [PubMed: 20026645]

42. Niwa S, Tanaka Y & Hirokawa N KIF1Bbeta- and KIF1A-mediated axonal transport of presynaptic regulator Rab3 occurs in a GTP-dependent manner through DENN/MADD. Nat Cell Biol 10, 1269–1279 (2008). [PubMed: 18849981]

43. Matanis T, Akhmanova A, Wulf P, Del Nery E, Weide T, Stepanova T, Galjart N, Grosveld F, Goud B, De Zeeuw CI, Barnekow A & Hoogenraad CC Bicaudal-D regulates COPI-independent Golgi-ER transport by recruiting the dynein-dynactin motor complex. Nat Cell Biol 4, 986–992 (2002). [PubMed: 12447383]

METHODS AND EXTENDED DATA REFERENCES

44. Sui H & Downing KH Structural basis of interprotofilament interaction and lateral deformation of microtubules. Structure (London, England : 1993) 18, 1022–1031 (2010).

45. Pettersen EF, Goddard TD, Huang CC, Couch GS, Greenblatt DM, Meng EC & Ferrin TE UCSF Chimera–a visualization system for exploratory research and analysis. J Comput Chem 25, 1605–1612 (2004). [PubMed: 15264254]

46. Charrier J-D, Miller A, Kay DP, Brenchley G, Twin HC, Collier PN, Ramaya S, Keily SB, Durrant SJ, Knegtel RMA, Tanner AJ, Brown K, Curnock AP & Jimenez J-M Discovery and structure-activity relationship of 3-aminopyrid-2-ones as potent and selective interleukin-2 inducible T-cell kinase (Itk) inhibitors. J Med Chem 54, 2341–2350 (2011). [PubMed: 21391610]

47. Woehlke G, Ruby AK, Hart CL, Ly B, Hom-Booher N & Vale RD Microtubule interaction site of the kinesin motor. Cell 90, 207–216 (1997). [PubMed: 9244295]

48. Suloway C, Pulokas J, Fellmann D, Cheng A, Guerra F, Quispe J, Stagg S, Potter CS & Carragher B Automated molecular microscopy: the new Leginon system. J Struct Biol 151, 41–60 (2005). [PubMed: 15890530]

49. Zheng SQ, Palovcak E, Armache J-P, Verba KA, Cheng Y & Agard DA MotionCor2: anisotropic correction of beam-induced motion for improved cryo-electron microscopy. Nature Methods 14, 331–332 (2017). [PubMed: 28250466]

50. Lander G, Stagg S, Voss N, Cheng A, Fellmann D, Pulokas J, Yoshioka C, Irving C, Mulder A & Lau P Appion: an integrated, database-driven pipeline to facilitate EM image processing. J Struct Biol 166, 95–102 (2009). [PubMed: 19263523]

51. Roseman AM FindEM–a fast, efficient program for automatic selection of particles from electron micrographs. J Struct Biol 145, 91–99 (2004). [PubMed: 15065677]

52. Zivanov J, Nakane T, Forsberg B, Kimanius D, Hagen WJH, Lindahl E & Scheres SHW New tools for automated high-resolution cryo-EM structure determination in RELION-3. eLife 7, (2018).

53. Punjani A, Rubinstein JL, Fleet DJ & Brubaker MA cryoSPARC: algorithms for rapid unsupervised cryo-EM structure determination. Nature Methods (2017).

54. Henderson R, Sali A, Baker ML, Carragher B, Devkota B, Downing KH, Egelman EH, Feng Z, Frank J, Grigorieff N, Jiang W, Ludtke SJ, Medalia O, Penczek PA, Rosenthal PB, Rossmann MG, Schmid MF, Schröder GF, Steven AC, Stokes DL, Westbrook JD, Wriggers W, Yang H, Young J, Berman HM, Chiu W, Kleywegt GJ & Lawson CL Outcome of the first electron microscopy validation task force meeting in Structure (London, England : 1993) 205–214 (MRC Laboratory of Molecular Biology, Hills Road, Cambridge CB2 0QH, UK., 2012).

55. Scheres SHW & Chen S Prevention of overfitting in cryo-EM structure determination. Nature Methods 9, 853–854 (2012). [PubMed: 22842542]

56. Rosenthal PB & Henderson R Optimal determination of particle orientation, absolute hand, and contrast loss in single-particle electron cryomicroscopy. J Mol Biol 333, 721–745 (2003). [PubMed: 14568533]
57. Chen S, McMullan G, Faruqi AR, Murshudov GN, Short JM, Scheres SHW & Henderson R High-resolution noise substitution to measure overfitting and validate resolution in 3D structure determination by single particle electron cryomicroscopy. Ultramicroscopy 135C, 24–35 (2013).
58. Wang RY-R, Song Y, Barad BA, Cheng Y, Fraser JS & DiMaio F Automated structure refinement of macromolecular assemblies from cryo-EM maps using Rosetta. eLife 5, 352 (2016).
59. Emsley P & Cowtan K Coot: model-building tools for molecular graphics. Acta Crystallographica Section D: Biological Crystallography 60, 2126–2132 (2004). [PubMed: 15572765]
60. Söding J, Biegert A & Lupas AN The HHpred interactive server for protein homology detection and structure prediction. Nucleic Acids Res 33, W244–8 (2005). [PubMed: 15980461]
61. Greggio E, Taymans J-M, Zhen EY, Ryder J, Vancraenenbroeck R, Beilina A, Sun P, Deng J, Jaffe H, Baekelandt V, Merchant K & Cookson MR The Parkinson's disease kinase LRRK2 autophosphorylates its GTPase domain at multiple sites. Biochemical and Biophysical Research Communications 389, 449–454 (2009). [PubMed: 19733152]
62. Wagner T, Merino F, Stabrin M, Moriya T, Antoni C, Apelbaum A, Hagel P, Sitsel O, Raisch T, Prumbaum D, Quentin D, Roderer Daniel, Tacke S, Siebolds B, Schubert E, Shaikh TR, Lill P, Gatsogiannis C & Raunser S SPHIRE-crYOLO is a fast and accurate fully automated particle picker for cryo-EM. Communications Biology 2, (2018).
63. Lis P, Burel S, Steger M, Mann M, Brown F, Diez F, Tonelli F, Holton JL, Ho PW, Ho S-L, Chou M-Y, Polinski NK, Martinez TN, Davies P & Alessi DR Development of phospho-specific Rab protein antibodies to monitor in vivo activity of the LRRK2 Parkinson's disease kinase. Biochem J 475, 1–22 (2018). [PubMed: 29127256]
64. Nicholas MP, Rao L & Gennerich A An improved optical tweezers assay for measuring the force generation of single kinesin molecules. Methods Mol Biol 1136, 171–246 (2014). [PubMed: 24633799]
65. Htet ZM, Gillies JP, Baker RW, Leschziner AE, DeSantis ME & Reck-Peterson SL LIS1 promotes the formation of activated cytoplasmic dynein-1 complexes. Nat Cell Biol 22, 518–525 (2020). [PubMed: 32341549]
66. Kendrick AA, Dickey AM, Redwine WB, Tran PT, Vaites LP, Dzieciatkowska M, Harper JW & Reck-Peterson SL Hook3 is a scaffold for the opposite-polarity microtubule-based motors cytoplasmic dynein-1 and KIF1C. J Cell Biol 218, 2982–3001 (2019). [PubMed: 31320392]

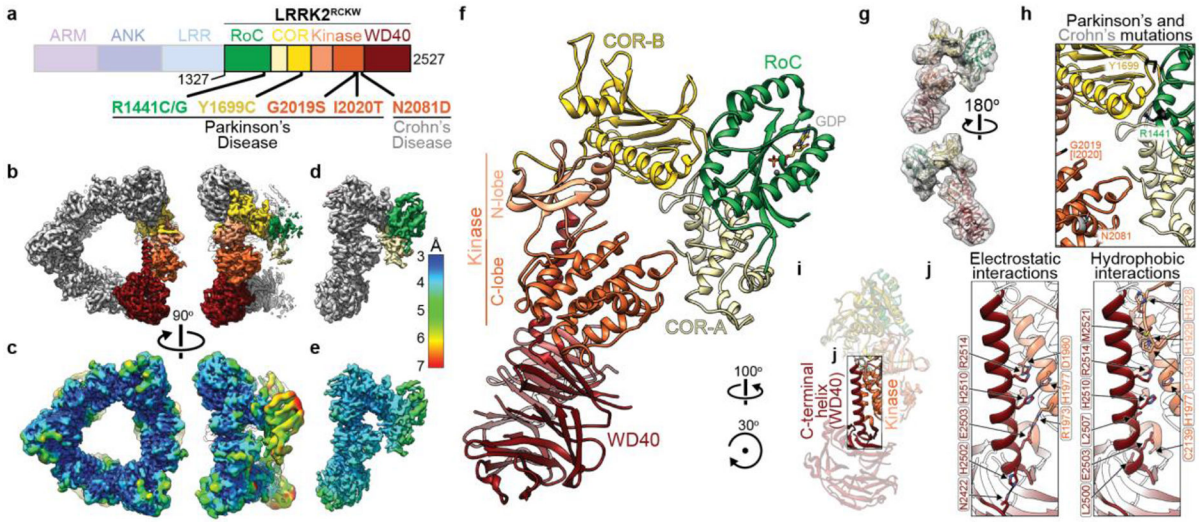

Figure 1 |. Cryo-EM structure of LRRK2^{RCKW}.

a, Schematic of the construct used in this study. The N-terminal half of LRRK2, absent from our construct, is shown in dim colors. The same color-coding of domains is used throughout the paper. The five major familial Parkinson's Disease mutations and a Crohn's Disease-linked mutation are indicated. **b**, **c**, 3.5Å cryo-EM map (b) and local resolution (c) of the LRRK2^{RCKW} trimer, with one monomer highlighted. **d**, **e**, 3.8Å cryo-EM map (d) and local resolution (e) of a LRRK2^{RCKW} monomer with improved resolution for the RoC and COR-A domains. **f**, Ribbon diagram of the atomic model of LRRK2^{RCKW}. **g**, 8.1Å cryo-EM map of monomeric LRRK2^{RCKW} with the model in (f) docked in. **h**, Location of the Parkinson's and Crohn's Disease mutations listed in (a). **i, j**, Interface between the C-terminal helix and the kinase domain in LRRK2^{RCKW} with residues involved in electrostatic and hydrophobic interactions indicated.

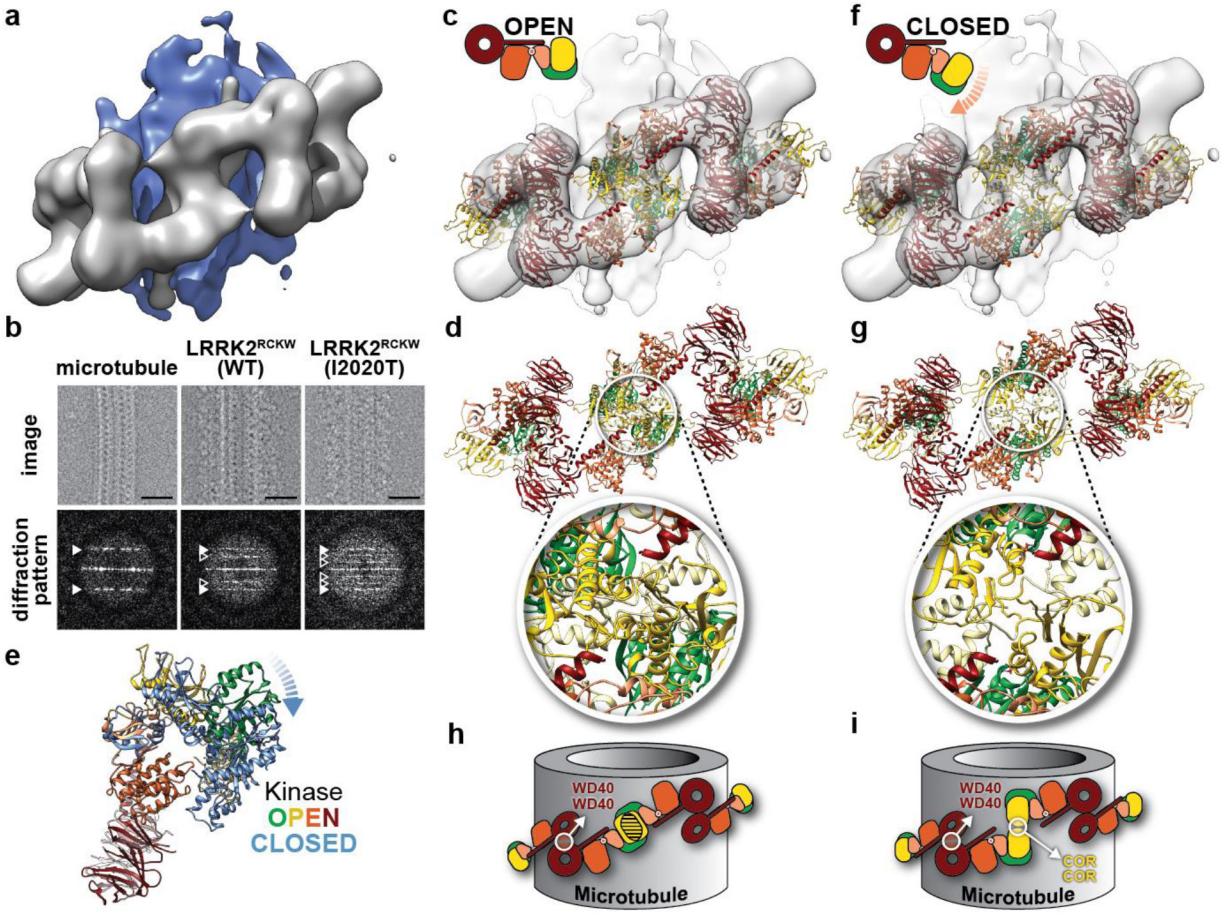

Figure 2 |. Modeling the microtubule-associated LRRK2 filaments.

a, 14Å cryo-ET map of a segment of microtubule-associated LRRK2 filament in cells. The microtubule is shown in blue and the LRRK2 filament in grey. **b**, Microtubule-associated LRRK2^{RCKW} filaments reconstituted *in vitro* from purified components. (Top) Single cryo-EM images of a naked microtubule (left), and WT (center) and I2020T (right) LRRK2^{RCKW} filaments. (Bottom) Diffraction patterns (power spectra) calculated from the images above. White and hollow arrowheads indicate the layer lines corresponding to the microtubule and LRRK2^{RCKW}, respectively. Scale bar: 20nm **c**, Fitting of the LRRK2^{RCKW} structure, which has its kinase in an open conformation, into the cryo-ET map. **d**, Atomic model of the LRRK2^{RCKW} filaments from (c). The white circle highlights the filament interface mediated by interactions between COR domains, where clashes are found. **e**, Superposition of the LRRK2^{RCKW} structure (colored by domains) and a model of LRRK2^{RCKW} with its kinase in a closed conformation in blue. The dashed blue arrow indicates the closing of the kinase. **f**, Fitting of the closed-kinase model of LRRK2^{RCKW} into the cryo-ET map. **g**, Atomic model of the closed-kinase LRRK2^{RCKW} filaments (g) with a white circle highlighting the same interface as in (d). **h, i,** Cartoon representation of the two filament models, highlighting the clashes observed with open-kinase LRRK2^{RCKW} (h) and resolved with the closed-kinase model (i). 82% of clashes were resolved using the closed-kinase LRRK2^{RCKW} model (see Methods for details).

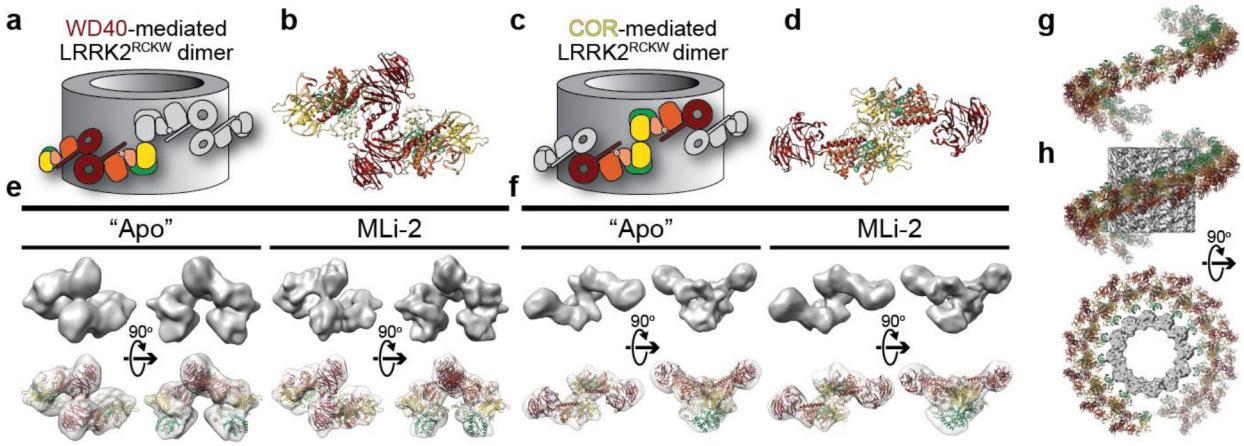

Figure 3 |. LRRK2^{RCKW} forms WD40- and COR-mediated dimers outside the filaments.

a-d, The filament model shown in Fig. 2j, k is shown here in grey, with either a WD40-mediated (a), or COR-mediated (c) LRRK2^{RCKW} dimer highlighted with domain colors. The corresponding molecular models are shown next to the cartoons (b, d). **e, f,** Cryo-EM reconstructions of LRRK2^{RCKW} dimers obtained in the absence of inhibitor ("Apo"), or in the presence of MLi-2. For each reconstruction, two orientations of the map are shown: down the two-fold axis at the dimerization interface (left), which matches the orientation of the models shown in (b, d), and perpendicular to it (right). The top row shows the cryo-EM map and the bottom row a transparent version of it with a model docked in. **g,** Molecular models of the WD40-mediated and COR-mediated LRRK2^{RCKW} dimers obtained in the presence of MLi-2 (e, f) were aligned in alternating order. This panel shows the resulting right-handed helix. **h,** The helix has dimensions compatible with the diameter of a 12-protofilament microtubule (EMD-5192)[44], which was the species used to obtain the cryo-ET map shown in Fig. 2a[5], and has its RoC domains pointing towards the microtubule surface.

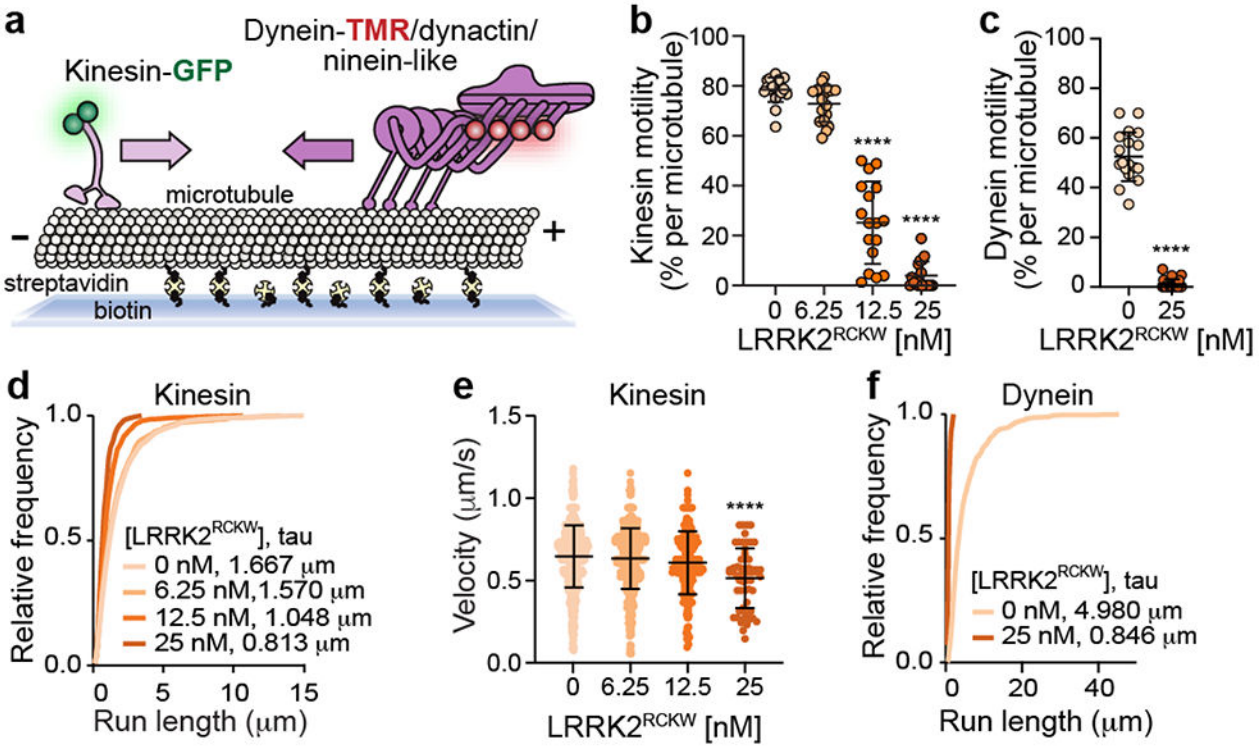

Figure 4 |. LRRK2^{RCKW} inhibits the motility of kinesin and dynein.

a, Schematic of the single-molecule motility assay. **b**, **c**, The percentage (mean ± s.d.) of motile events per microtubule as a function of LRRK2^{RCKW} concentration for kinesin (b) and dynein (c). ****$p < 0.0001$ (Kruskal-Wallis test with Dunn's posthoc for multiple comparisons for (b)) and ****$p < 0.0001$ (Mann Whitney test) for (c)). **d,** Cumulative frequency distribution of kinesin run lengths as a function of LRRK2^{RCKW} concentration. Mean decay constants (tau) are shown. The 12.5 nM and 25 nM, but not 6.25 nM, conditions were significantly different ($p < 0.0001$) than the 0 nM condition (one-way ANOVA with Dunnett's test for multiple comparisons using error generated from a bootstrapping analysis). **e**, Velocity of kinesin as a function of LRRK2^{RCKW} concentration. Data are mean ± s.d. ****$p < 0.0001$ (one-way ANOVA with Dunn's posthoc for multiple comparisons). **f,** Cumulative frequency distribution of dynein run lengths as a function of LRRK2^{RCKW} concentration. Mean decay constants (tau) are shown. Data was resampled with bootstrapping analysis and was significant. $p < 0.0001$ (unpaired t-test with Welch's correction using error generated from a bootstrapping analysis).

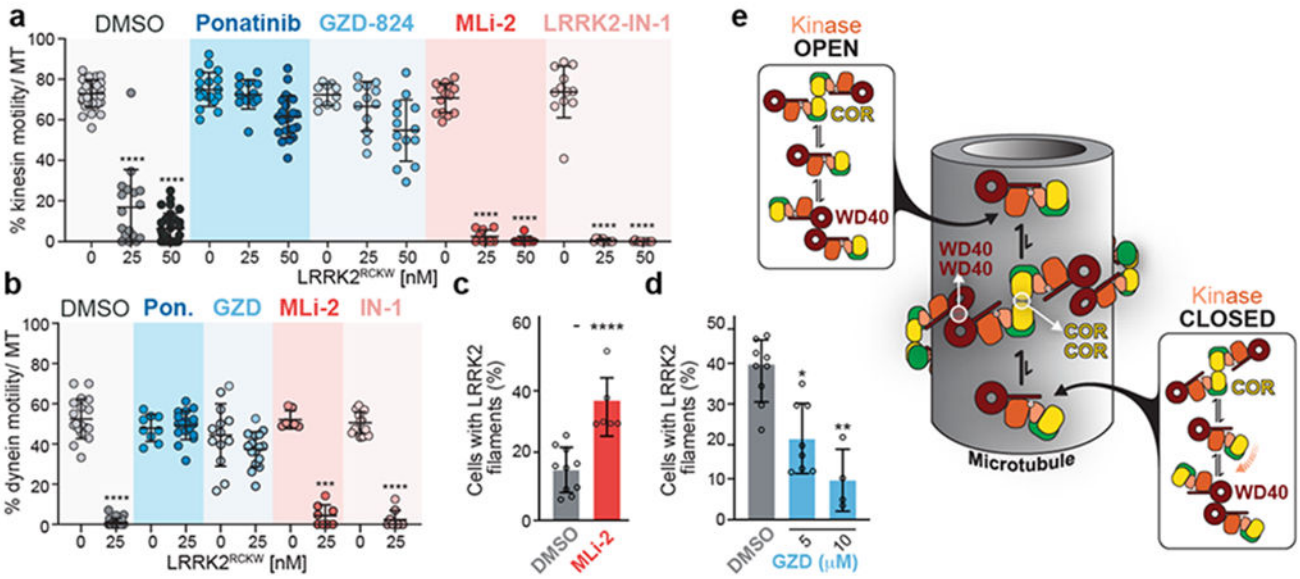

Figure 5 | Type II, but not Type I, kinase inhibitors rescue kinesin and dynein motility and reduce LRRK2 filament formation in cells.

a, b, Effects of different kinase inhibitors on LRRK2^{RCKW}'s inhibition of kinesin (a) and dynein (b) motility. Data shown is the percentage of motile events per microtubule (MT) as a function of LRRK2^{RCKW} concentration in the absence (DMSO) or presence of the indicated inhibitors (Ponatinib and GZD-824: 10 μM; MLi-2 and LRRK2-IN-1: 1 μM). Data are mean ± s.d. ***p < 0.001 and ****p < 0.0001 (Kruskal-Wallis test with Dunn's posthoc for multiple comparisons within drug only). **c**, Treatment with MLi-2 (500 nM) for 2 hrs increases WT GFP-LRRK2 filament formation in 293T cells. Data are mean ± s.d. ****p=0.0002 (Mann Whitney test). **d,** Treatment with GZD-824 (5 μM) for 30 mins decreases GFP-LRRK2 (I2020T) filament formation in 293 cells. Data are mean ± s.d. *p=0.0133 and **p=0.0012 (Kruskal-Wallis with Dunn's posthoc test for multiple comparisons). **e,** Schematic representation of our hypothesis. LRRK2's kinase can be in an open or closed conformation. The different species we observed are represented in the rounded rectangles, but only monomers are shown on the microtubule for simplicity. Our model proposes that the kinase-closed form of LRRK2 favors oligomerization on microtubules.